creative commons
COMMONS DEED

저작자표시-비영리-동일조건변경허락 2.0 대한민국

이용자는 아래의 조건을 따르는 경우에 한하여 자유롭게

- 이 저작물을 복제, 배포, 전송, 전시, 공연 및 방송할 수 있습니다.
- 이차적 저작물을 작성할 수 있습니다.

다음과 같은 조건을 따라야 합니다:

저작자표시. 귀하는 원저작자를 표시하여야 합니다.

비영리. 귀하는 이 저작물을 영리 목적으로 이용할 수 없습니다.

동일조건변경허락. 귀하가 이 저작물을 개작, 변형 또는 가공했을 경우에는, 이 저작물과 동일한 이용허락조건하에서만 배포할 수 있습니다.

- 귀하는, 이 저작물의 재이용이나 배포의 경우, 이 저작물에 적용된 이용허락조건을 명확하게 나타내어야 합니다.
- 저작권자로부터 별도의 허가를 받으면 이러한 조건들은 적용되지 않습니다.

저작권법에 따른 이용자의 권리는 위의 내용에 의하여 영향을 받지 않습니다.

이것은 이용허락규약(Legal Code)을 이해하기 쉽게 요약한 것입니다.

Disclaimer

dCollection

재료공학 석사학위논문

First-principles study on point defects in hematite (α-Fe_2O_3)

헤마타이트(α-Fe_2O_3)에서의 점결함에 대한 제일원리 연구

2013년 2월

서울대학교 대학원

공과대학 재료공학부

이주희

First-principles study on point defects in hematite (α-Fe_2O_3)

헤마타이트(α-Fe_2O_3)에서의 점결함에 대한 제일원리 연구

지도교수 한 승 우

이 논문을 재료공학 석사학위논문으로 제출함

2013년 2월

서울대학교 대학원

공과대학 재료공학부

이 주 희

이주희의 석사학위논문을 인준함

2013년 1월

위 원 장 남 기 태 (인)

부 위 원 장 강 기 석 (인)

위 원 한 승 우 (인)

Abstract

First-principles study on point defects in hematite

Joohee Lee

Department of Materials Science and Engineering

The Graduate School

Seoul National University

Hematite (α-Fe_2O_3) is receiving much attentions recently for the application to solar water splitting, because it is stable in water like other oxide materials and abundant on the earth crust. In addition, Fe_2O_3 has a low band gap (2 eV) which enables absorbtion of wide spectrum of sunlight. However, the first-principles study on this material is not sufficient yet. In particular, few studies have been done on the point defects although the material property critically depends on the presence of native defects.

In this study, we carry out GGA+U calculations to investigate point defects in Fe_2O_3. In particular, we consider vacancies and interstitial defects of oxygen and iron, on which we determine relative stability by computing formation energies. The cell-size dependence of charged defects is carefully tested. The defect levels associated with each

defect are examined and explained on the basis of bulk electronic structure, and we also consider electron polaron in defect-free structure. Subsequently, the transition levels of charged states are computed and we determine the defect densities and Fermi level positions by the charge neutrality condition. It is found that the intrinsic defects generally lead to *n*-type condition, which is mainly driven by Fe interstitial defects. This is consistent with the fact that Fe_2O_3 is used as photoanode in water splitting owing to its intrinsic *n*-type property. Interestingly, we find that the Fermi level in *n*-type condition is pinned to 0.55 eV below the conduction band minimum by the formation of electron polaron.

Keywords : density functional theory (DFT), point defect, hematite(α -Fe_2O_3), water splitting

Student Number : 2011-20662

Contents

List of table and figures

CHAPTER 1

Introduction

Various measures of global security indicate that the world is heading toward an energy crisis. Many efforts are given to finding the best solution in the form of the renewable energy. Hydrogen gas is an extremely good energy source for clean energy system like fuel cells. At the present time, however, hydrogen gas is produced from fossil fuel emitting CO_2, which have to be replaced to renewable energy system without emission of environment contaminants. In this sense, solar water splitting has been given much attention as the method to utilizes the solar energy to generate hydrogen gases.

Solar water splitting is realized by following processes. (i) Absorption of photons to generate electron-hole pair. (ii) Charge separation and migration of photoexcited electronic carriers. Finally, (iii) sufficient potentials of photoexcited carriers for water splitting and the existence of active sites. For (i) and (iii), band levels are important as illustrated in Fig. 1. For the former process, band gap has to be narrow to absorb a wide range of light spectrum including visual light. For latter process on the other hand, the conduction band minimum has to be upper than the redox potential of H^+/H_2 (0 V with reference to NHE) and the valence band maximum has to be lower than the redox potential of O_2/H_2O (1.23 V), therefore the minimum band gap for water splitting is 1.23 eV. Fig. 2 shows band levels of various

semiconductor materials. Although CdS seems to have a suitable band alignment, it experiences photocorrosion making it not active for water splitting.

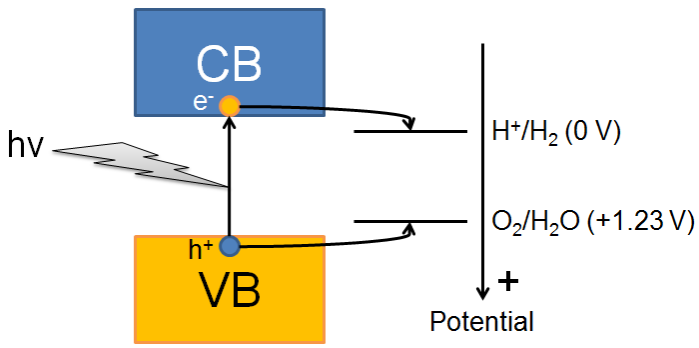

Fig. 1 Principle of water splitting. CB and VB means conduction band and valence band respectively. e^-, h^+ represent photoexcited electron and hole.

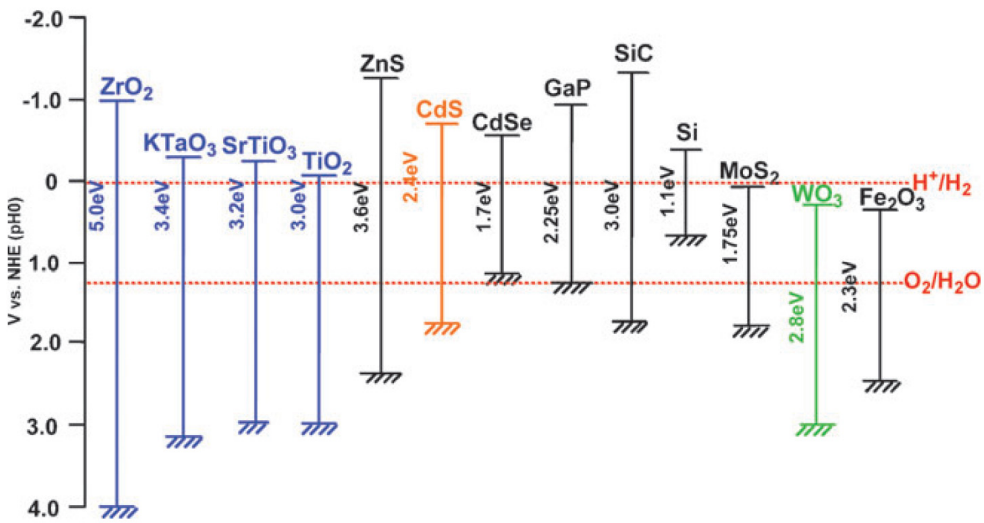

Fig. 2 Band levels of various semiconductor as compared with redox potentials of water splitting.[23]

Among the semiconductors in Fig. 2, hematite (α-Fe_2O_3) is a promising material enabling the water splitting owing to several advantages including proper band gap for light absorption, stability in water, and also the abundance in earth crust. In addition, Fe_2O_3 is a good photocatalyst for O_2 evolution because the photogenerated holes have sufficient potentials due to its low valence band level, although it is not active for H_2 evolution due to its low conduction band level. Therefore, for now, Fe_2O_3 is used as a photoanode for water splitting. The water splitting system using photoanode and photocathode is shown in Fig. 3.

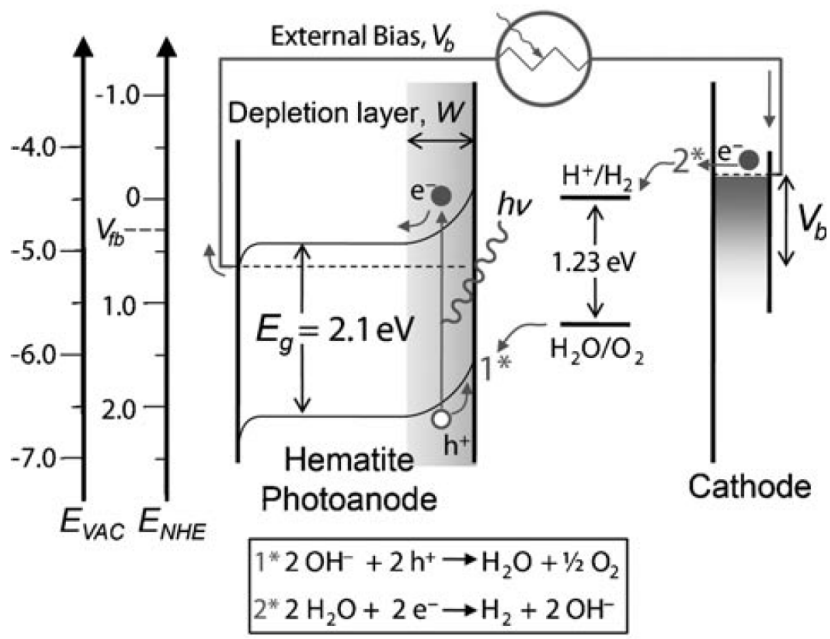

Fig. 3 Schematic diagram for water splitting system using photoanode (Fe_2O_3) and photocathode. E_g, V_{fb}, and V_b indicate the photoanode band gap, flat band potential, and the applied bias, respectively.[24]

However, the application of Fe_2O_3 for water splitting has some challenges. (i) Low flat band potential, V_{fb}, compared with the hydrogen reduction potential, (ii) required overpotential for oxidation of water to evolve O_2 gas which can be seen in Fig. 3, and (iii) poor carrier mobility. (i) and (ii) are improved by surface modification methods, and (iii) can be enhanced by morphology control.[24] By these optimizing methods, however, an impressive reports of activity have not appeared. This is thought to be caused by presence of defects or by-produced oxide near the interface. For more accurate control or optimization, knowledge about physical properties of the material including defects have to be supported.

However, intrinsic properties of the Fe_2O_3 have not been studied well within the atomic scales. Especially, the point defect studies are not in much progress particularly at the first-principles level even though the presence of native point defects is closely related to the properties of oxide materials.

The defect controled behavior is often discussed with experimental measurement of the conductivity which changes with respect to the non-stoichiometry condition or oxygen partial pressure in equilibrium. It was found that the iron oxide becomes oxygen-deficient at high temperatures in air and the donor centers keep remaining during cooling, but whether non-stoichiometric iron oxide contains oxygen vacancies or interstitial cations, and which kind of defects among them are involved in the *n*-type conductivity are not known.[1] People thought the oxygen vacancy as the main cause because intrinsic *n*-type

conductivity have been most generally attributed to oxygen vacancies in oxide materials. However, there is no clear evidence about that due to the difficulty of distinction by experimental methods. On the other hand, they also said that the p-type conductivity is obtained only over 1000℃[1], but the acceptor center is not defined yet. Furthermore, the explanation to the issue of low carrier mobility is scarce especially in the perspective of native point defect.

We studied the intrinsic point defects to explain or resolve the problems mentioned above, thus we can control the material properties for water splitting application like carrier densities, defect densities and band alignment by changing the condition of fabrication environment. We will discuss the applicability of intrinsic Fe_2O_3 for the purpose of water splitting by this study.

It was found that the non-stoichiometry of Fe_2O_3 is caused by the oxygen vacancies which have low formation energy, but they cannot contribute much in the *n*-type conductivity due to its deep nature. The shallow Fe interstitial was more dominant to the *n*-type property. Explanation about the low carrier mobility, and possible range of band alignment will be also discussed.

CHAPTER 2

Theoretical background

2.1. First-principles calculation : density functional theory [2]

Currently, most of the electronic structure calculations of materials have been based on the density functional theory, DFT. One of the main points of DFT is Hohenberg-Kohn theorem which implies that the ground state density is the necessary and sufficient information to calculate the electronic structure of materials and corresponding total energies. Another point is that the theory make it possible that an accurate but practically unsolvable Schrödinger equation is substituted by the effective one-electron equation (called "Kohn-Sham equation" Eq.(1)).

$$\left[-\frac{\hbar^2}{2m_e}\nabla^2 + V_{ext}(\vec{r}) + V_H(\vec{r}) + V_{xc}(\vec{r})\right]\psi_i(\vec{r}) = \varepsilon_i\psi_i(\vec{r}) \quad . \qquad (1)$$

Kohn-Sham Hamiltonian shown in the left side of Eq.(1) is composed of kinetic energy term, external potential term, Hartree, and exchange-correlation potential terms. The Kohn-Sham density functional theory is usually used for self-consistent-field calculations of the ground-state properties.[3]

DFT is accurate in principle, but actually some approximation like LDA or GGA is applied to describe the exchange-correlation term. These

approximations have a well-known error called “self-interaction error“ that occurs because the Hartree potential and exchange-correlation potential terms are not canceled exactly. Generally speaking, this error is also can be understood by delocalization error. Therefore, first-principles calculations of Fe_2O_3, for example, give a wrong electronic ground state in LDA or GGA because strongly localized Fe *d* electron undergoes large self-interaction error, so we have to use other methods such as DFT+*U* or those with the hybrid functional. In this study, we used the DFT+*U* method and the results were quite reasonable.

2.2. Exchange-correlation functional

2.2.1. Local density approximation (LDA)

The local-density approximation (LDA) is an approximation scheme to deal with the exchange-correlation term in Kohn-Sham equation introduced by Kohn and Sham.[4] The LDA assumes that the exchange-correlation energy of the system as a functional of charge density function that it is identical to that of the homogeneous electron gas which have same local density, so the exchange-correlation term depends on local density of the system only, like follows.

$$E_{xc}^{LDA}[\rho(r)] = \int \varepsilon_{xc}^{LDA}(\rho(r))\rho(r)dr \,, \tag{2}$$

where $\varepsilon_{xc}^{LDA}(\rho(r))$ is the exchange-correlation energy density of the homogeneous system as mentioned above.

The LDA might be most adequate for systems that have smooth electron density such as the free electron like metal or the semiconductor. However, using it to the systems that have rapidly changing electron density such as the transition metal systems which have the localized electrons could possibly include error. Usually, the bond strength or the lattice parameter is underestimated than experiment.

2.2.2. Generalized gradient approximation (GGA)

The LDA could imply large errors for the system where the electron density changes rapidly, because LDA sees only that point of electron density to evaluate the exchange-correlation energy term. Therefore, generalized gradient approximation (GGA) which considers also the gradient of electron density of the local point is introduced later on by Perdew[3] and Becke[5]. In this case, the exchange-correlation energy is expressed by the equation below.

$$E_{xc}^{GGA}\left[\rho(r),\nabla\rho(r)\right]=\int\varepsilon_{xc}^{GGA}(\rho(r),|\nabla\rho(r)|)\rho(r)dr \quad (3)$$

This improved approximation solves certain extent of errors of LDA that it describes more accurately for the physical properties like bond strength. Especially, the improvement for materials with rapidly changing electron density could be significant.

2.2.3. DFT+U

Despite the further improvement in GGA than LDA, the GGA cannot describe well for strongly correlated materials that have d or f orbital. To solve this problem, DFT+U formalism is developed by Liechtenstein et al. [6]

The DFT+U formalism treat the averaged Coulomb interaction with the on-site Coulomb interaction (Hubbard-like term).

$$E_{local}^{DFT+U} = E^{DFT} + \frac{1}{2}U\sum_{i\neq j}\rho_i\rho_j - E^{ee},$$

$$E^{ee} = \frac{UN^2}{2} - \frac{1}{2}\sum_{\sigma}N_{\sigma}^2 - \frac{1}{2}(U-J)\sum_{\sigma,m}n_{m,\sigma}^2 . \quad (4)$$

It uses the orbital-dependent potential represented by empirical parameters called U and J, which is Hubbard term and exchange term respectively. The term of E^{ee} in Eq.(4) effectively cancels double-counting of Coulomb interaction, where U is defined as the loss of Coulomb energy when two electron occupy the same orbital which expressed as Eq.(5), and J is related to the exchange interaction of spins when two electron occupy the same orbital.

$$U = \left[E(d^{n+1}) + E(d^{n-1})\right] - 2E(d^n) . \quad (5)$$

The DFT+U gives improved results for strongly correlated systems with no additional time consuming, so we are using the DFT+U formalism in this study

CHAPTER 3

Result I : hematite (α -Fe_2O_3) crystal

3.1. Computational details

We carried out first-principles calculations with GGA+U functional using the Vienna Ab-initio Simulation Package (VASP) code[7] by the projected augmented wave (PAW) pseudo potential method.[8] The effective U parameter U_{eff} of 4.3 eV was used, which corresponds to U-J where U is Coulomb and J is exchange parameter.[9] Valence electrons of $4s^1 3d^7$ for Fe, and $2s^2 2p^4$ for oxygen were considered. The cutoff energy for plane-wave basis set is chosen to be 550 eV, and the k-space mesh grid is $4\times4\times4$ within Monkhorst-Pack scheme for primitive cell. Structures were relaxed until the Hellman-Feynman forces of all ions are less than 0.02 eV/Å. To compute dielectric constants (optical and static), a density functional perturbation theory implemented in VASP is used. For the calculations of defective supercells, cells expanded by $2\times2\times1$ with the conventional hexagonal unit cell (~120 atoms) was used, and $2\times2\times2$ Monkhorst-Pack k-points were sampled for those calculations.

3.2. Bulk property

Fe_2O_3 is a corundum-structured oxide like Al_2O_3 in which Fe ions occupy two thirds of octahedral interstitial sites. Fe_2O_3 is known to be antiferrimagnetic and becomes canted antiferromagnetic or weakly ferromagnetic above 250K (so called Morin transition). We consider various antiferromagnetic configurations of Fe atoms and the minimum energy (1.02 eV/primitive cell lower than the ferromagnetic solution.) is obtained when magnetic moments of Fe atoms within *xy* plane are aligned in parallel while the moment alternates along the *z* axis. (See Fig. 4.) This is consistent with other works[25~27]. The basic bulk properties computed within the present computational setup is displayed in Table 1. The agreement with experiment is reasonable.

Table 2 Bulk properties of Fe_2O_3

	Rhombohedral lattice constant (Å)	Rhombohedral angle (°)	Magnetic moment (μ_B)	Band gap (eV)
PBE+4.3	5.47	55.21	4.18	2.25
Expt.	5.43	55.23	4.9	2.0−2.2 (opt.) 2.6±0.4 (PES)

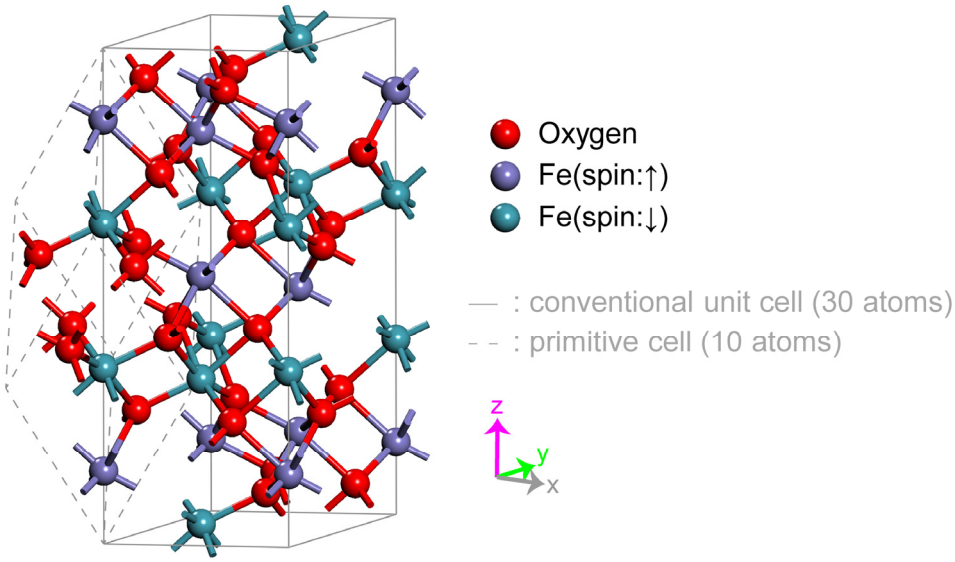

Fig. 4 Clean cell with ground magnetic configuration. Primitive and conventional unitcell is represented by gray dashed line, solid line, respectively. Red, blue, green spheres are oxygen, Fe with positive spin, and with negative spin.

The band structure and partial density of states (PDOS) of Fe_2O_3 are shown in Fig. 5 and 6. Figure 6 shows that the valence band is a mixture of O *p* and majority Fe *d* orbitals while the conduction band is mostly minority Fe *d* orbitals. That is to say, the energy gap of Fe_2O_3 is charge-transfer style as was confirmed by photoemission experiment. [11] We also decompose Fe *d* orbital into t_{2g} and e_g orbitals and the energy ordering in Fig. 6 is consistent with the well-known crystal field theory. The t_{2g} manifold is further divided into into a_{1g} and e_g^{π} by trigonal crystal field from the second-nearest neighbors of Fe, and to avoid confusion e_g will be written as e_g^{σ}. The shapes of these splitted orbitals can be found in Fig. 8. By comparing this with the Eigen functions in bulk Fe_2O_3, the schematic diagram could be estimated as in Fig. 9. We also represented the charge distributions of CBM and VBM in Fig. 7.

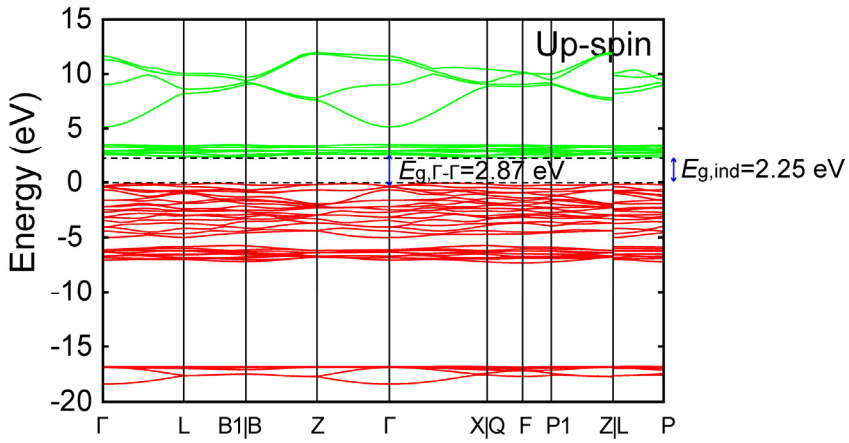

Fig. 5 Energy band structure of bulk Fe_2O_3. dashed lines indicate conduction band minimum (CBM), and valence band maximum. $E_{g,ind}$ is indirect band gap, and $E_{g,\Gamma-\Gamma}$ is direct band bap in Γ point.

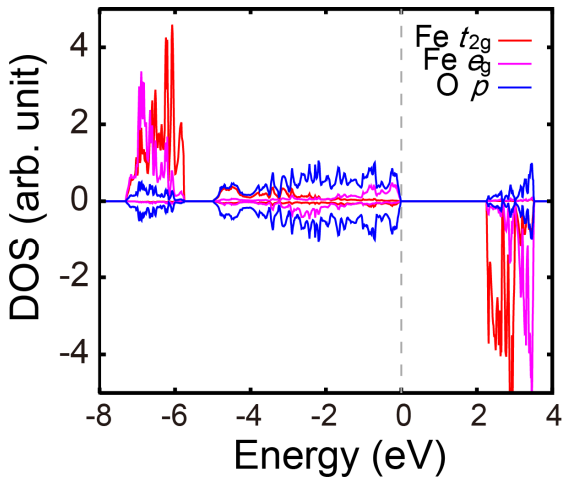

Fig. 6 Density of states (DOS) of bulk Fe_2O_3. red, magenta, blue lines represent projected density of states (DOS) of Fe t_{2g}, Fe e_g and O p, respectively. Dashed line indicates Fermi level.

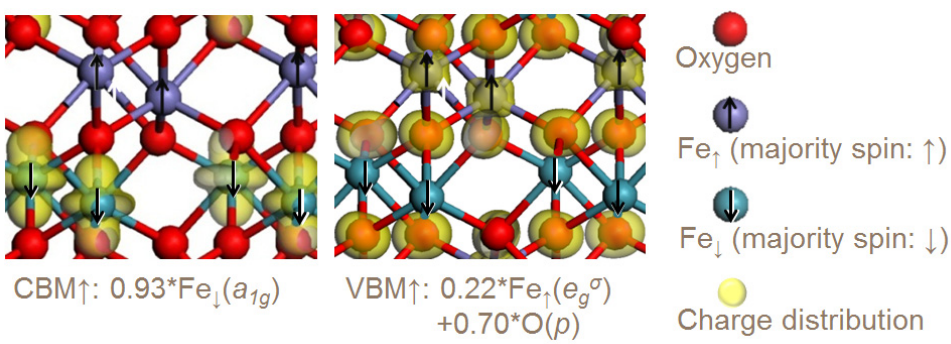

Fig. 7 Partial charges of CBM and VBM of bulk Fe_2O_3. Yellow surface displays charge distribution for conduction band minimum with positive spin (CBM↑), and valence band maximum with positive spin (VBM↑).

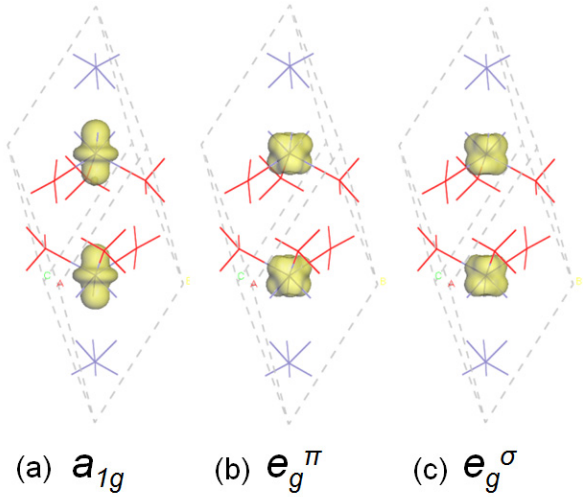

Fig. 8 Split of Fe *d* orbitals by crystal field. Dashed line shows primitive unitcell. Yellow surfaces are shape of corresponding orbital at Fe site. (a) a_{1g}, (b) e_g^{π}, and (c) e_g^{σ}

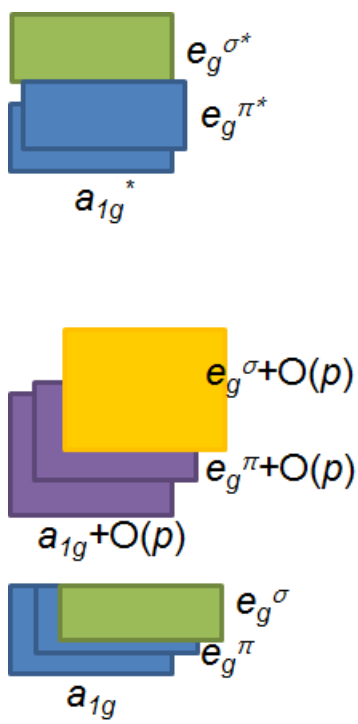

Fig. 9 Schematic diagram of band structure

CHAPTER 4

Result Ⅱ : intrinsic point defects in Fe_2O_3

As a first step to investigate point defects, we examine the electronic structure related to each neutral defect. We consider both vacancy and interstitial defects such as O vacancy (V_O), Fe vacancy (V_{Fe}), interstitial O (O_I) and interstitial Fe (Fe_I) atoms, and focus on the relaxation pattern and defect levels within the band gap. One type of point defect is created within $2\times2\times1$ supercell comprising 120 atoms.

4.1. Oxygen vacancy

4.1.1. V_O : relaxation patterns

All the oxygen atoms in Fe_2O_3 are surrounded by four Fe atoms in the above and below layers. (See Fig. 10a.) In the bulk structure, Fe-O bond lengths are 2.12 and 1.97 Å ("long" and "short" in Fig. 11a). When the oxygen atom is removed, neighboring Fe (O) atoms relax outward (inward) by ~0.15 (~0.1) Å. The donor centers of two electrons are formed at two first nearest ion site ($Fe_{\uparrow}^{s}$ and $Fe_{\downarrow}^{s}$, where subscript means direction of the majority spin of the atom) among the four neighboring tetrahedral Fe ions. In the case of V_O^{2+} configuration, the electrons at β state in Fig. 11b which are localized at $Fe_{\uparrow}^{s}$ and $Fe_{\downarrow}^{s}$ are unoccupied, thus the effect that was screening the effective

plus charge of V_O is reduced, thus the associated ions show further outward relaxations. (See Fig. 10.)

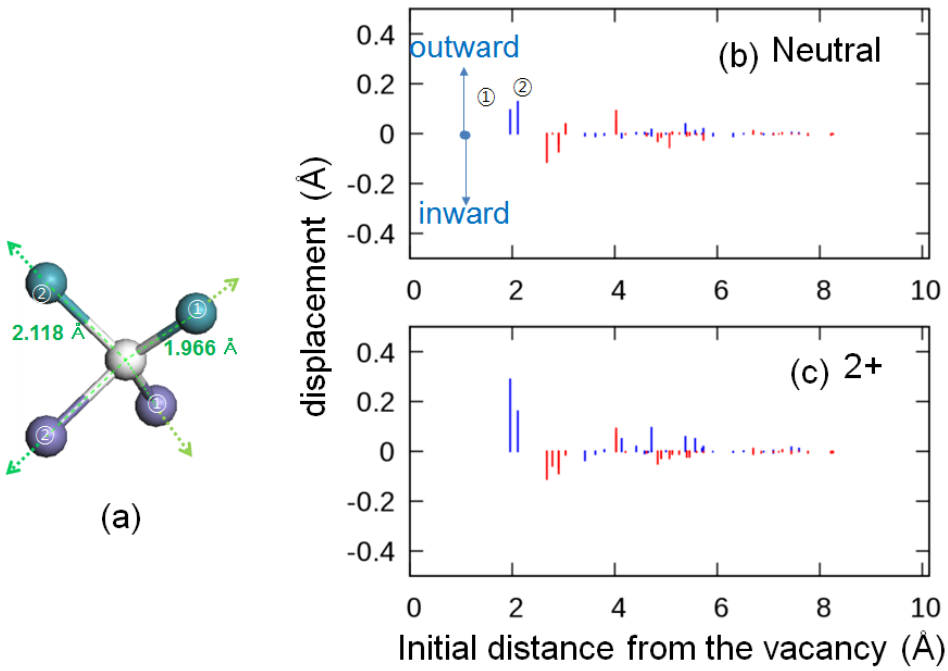

Fig. 10 (a) and (b), (c) display relaxation patterns and ionic displacements in oxygen vacant system with respect to the distance from the vacancy. It shows x-range up to the minimum distance between the defects of vicinity cells. (b) is for neutral V_O, (c) is for V_O^{2+}

4.1.2. V_O : electronic structure

The oxygen vacancy results in the spin-symmetric DOS and generates 3 defect levels in the band gap as denoted by α, β, and γ in Fig. 11b. The unoccupied α level is mostly Fe^{I} *d* orbital while the topmost occupied β level consists of mainly *d* orbitals of Fe^{S} atoms. Therefore, these states are similar to the conduction-band state in the bulk. The γ level is distributed rather broadly over nearby Fe and O atoms, meaning that it is the perturbed valence-band state. (The spatial distributions of the up-spin α, β, and γ states are shown in Fig. 11a.)

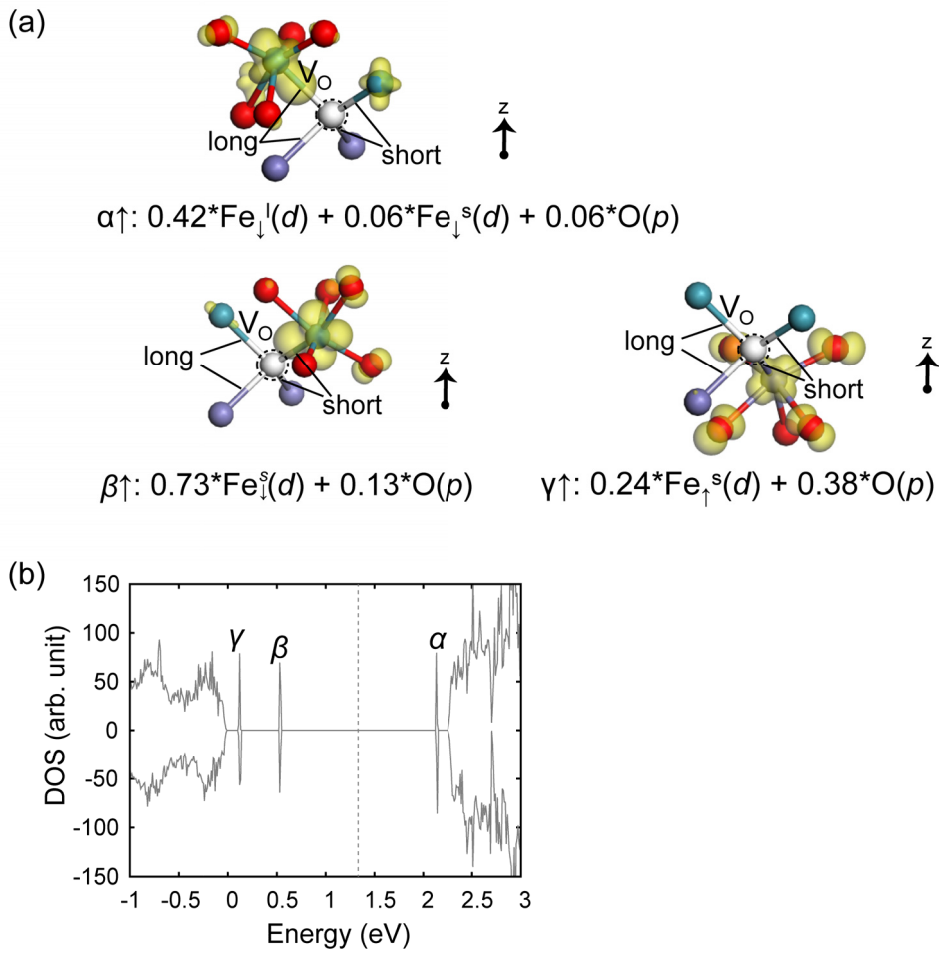

Fig. 11 (a) Partial charge distribution of defect states, and (b) DOS of the defective system with V_O.

4.2. Iron vacancy

4.2.1. V_{Fe} : relaxation patterns

In the case of iron atoms in Fe_2O_3, the surrounding consists of six O atoms in the above and below layers. (See Fig. 12a.) The bond lengths of Fe atoms with above O atoms are denoted by superscript *s* meaning short bond. (The Fe-O bond of Fe atoms in below layer is long) When the iron atom is removed, neighboring O (Fe) atoms relax outward (inward) by ~0.2 (~0.18) Å.

The size of defect is larger than that of V_O, as we can check in the distributions of relaxation in Fig. 12 where ions show larger displacement than in the system of V_O in Fig. 10. When the Fe ion is removed forming an V_{Fe}, the ion is carrying out $\alpha^1\uparrow, \alpha^2\uparrow, \beta^1\uparrow$ state electrons in Fig. 13, so O^ss relax outward more than O^ls to get rewarded from other Fe atoms for the missing electrons. When the vacancy is charged, the neighbor ions recover normal charges as in bulk; the displacements of O^ss and O^ls get similar with each other.

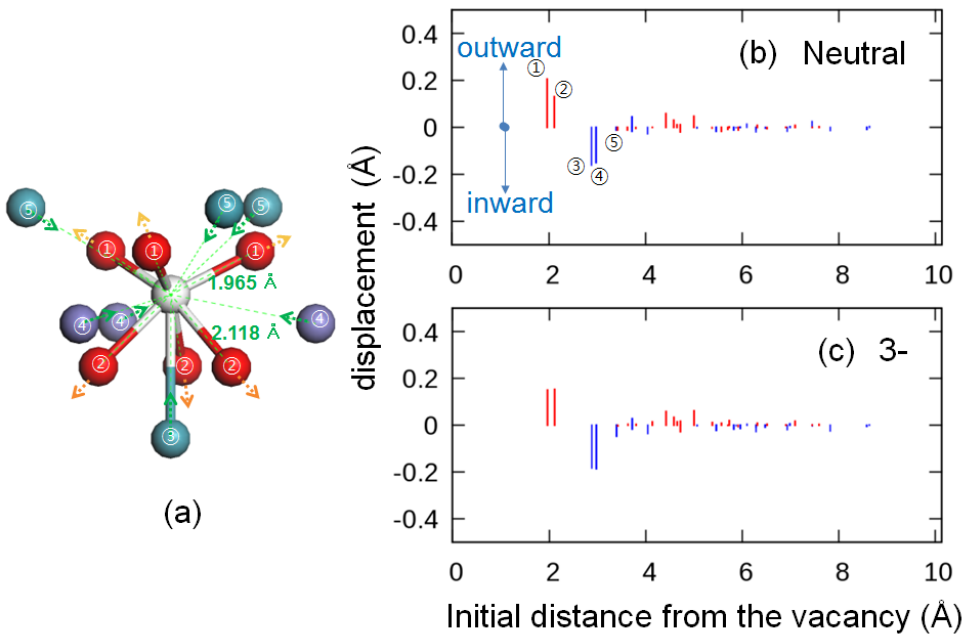

Fig. 12 (a) and (b),(c) display relaxation patterns and ionic displacements in Fe vacant system with respect to the distance from the vacancy. (b) is for neutral V_{Fe}, (c) is for V_{Fe}^{3-}

4.2.2. V_{Fe} : electronic structure

Fe vacancy induces shallow accepter levels of perturbed host states that resemble the VBM state but around the defect site. Especially, α states of which partial charge is distributed mainly on above layer are higher in energy level than β state on below layer. Because the V_{Fe} seems like shallow acceptor, intrinsic p-type character might be obtained by V_{Fe}.

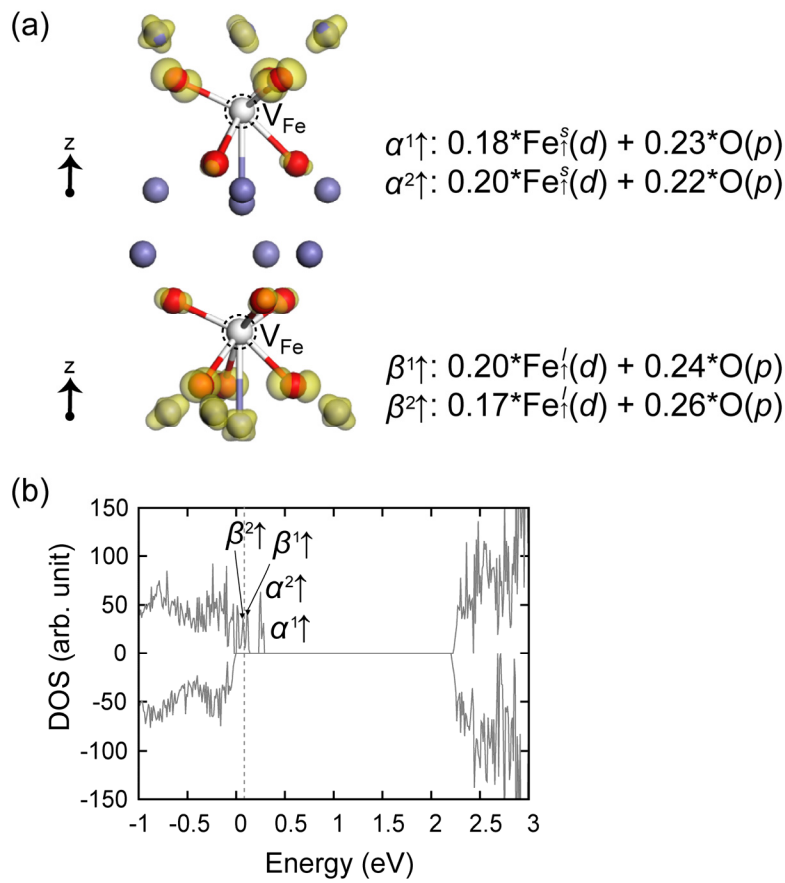

Fig. 13 (a) Partial charge distribution of defect states, and (b) DOS of the defective system with V_{Fe}.

4.3. Oxygen interstitial

To study interstitial defect, we have to consider the interstitial site first. There are six octahedral sites surrounded by oxygen in primitive cell of Fe_2O_3 in which four of the sites are occupied by iron atoms and two are vacant. The vacant sites are the interstitial sites in this system. On the other hand, O_I often found in dimer like form in several close-packed metal oxides and also called as split interstitial. [12] We considered octahedral interstitial and split interstitial. In the case of octahedral interstitial, open shell triplet state is most stable. In the case of split interstitial, closed-shell singlet state is most stable, and also it is the ground state that is lower by 0.1 eV per unit than the octahedral one. Therefore, we discuss the characters of the split interstitial in following chapters.

4.3.1. O_I : relaxation patterns

It is to notice that the relaxations are mostly outward regardless of the atomic species. It is because for interstitial, the space is tight around interstitial and it is dominant factor than the coulomb interaction, so the ions relax outward away.

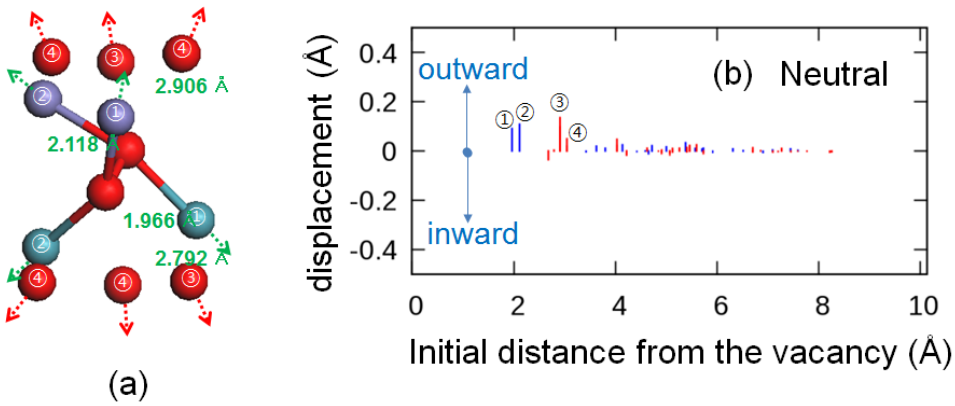

Fig. 14 (a) and (b) display relaxation patterns and ionic displacements in system with interstitial oxygen depending on the distance from the defect. (b) is for neutral split O_I.

4.3.2. O_I : electronic structure

The state α induced due to split O_I is vicinity of VBM having low energy levels. The spin-symmetric DOS is shown having the closed-shell singlet state. The defect is not charged because the occupied α level is far from the CBM showing deep character.

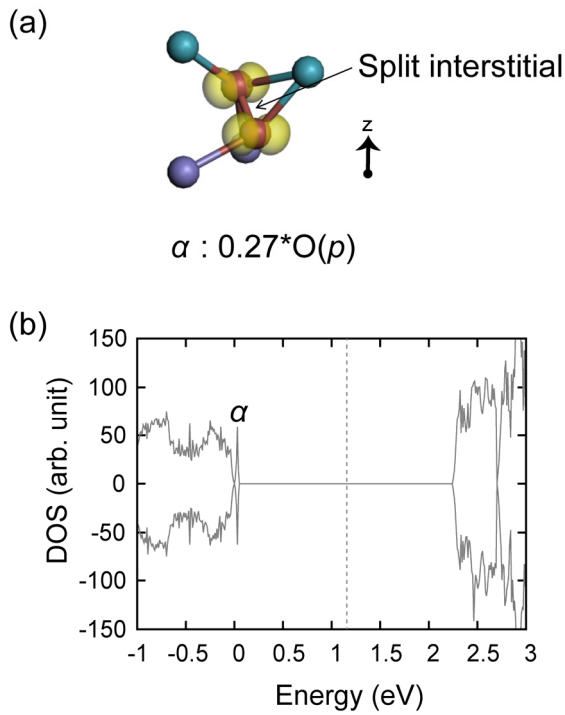

Fig. 15 (a) Partial charge distribution of defect states, and (b) DOS of the defective system with O_I.

4.4. Iron interstitial

We also carried out the site stability calculations, and the stable site was also found to be the octahedral interstitial (lower in energy by 0.2 eV/unit than the tetrahedral one) as known experimentally.[1] In addition, there are two cases depending on the majority spin of Fe_I. Considering interstitial site in the center of the primitive cell in Fig. 4, spin configurations of $\uparrow\downarrow(\downarrow)\downarrow\uparrow$ and $\uparrow\downarrow(\uparrow)\downarrow\uparrow$ along c axis are possible. As for neutral interstitial Fe atom, formal case is more stable. So, here we mainly show the formal case, but also show the electronic structure of latter case in Fig. 18.

4.4.1. Fe_I : relaxation patterns

The ions around the defect also show outward relaxation mostly, but neighboring oxygen ions show somewhat inward relaxation, because the site is looser than in the case of O_I, and Fe_I has positive charge that attracts the oxygen ions. For the positively charged Fe_I, additional electrons of nearest and next nearest neighbor Fe ions along c direction are removed (β and γ states in Fig. 17), and the corresponding ions show more outward relaxation (① and ③ ions in Fig. 16, and $Fe_{\downarrow}^{1F}$ and $Fe_{\uparrow}^{2F}$ ions in Fig. 17) due to larger positive charges.

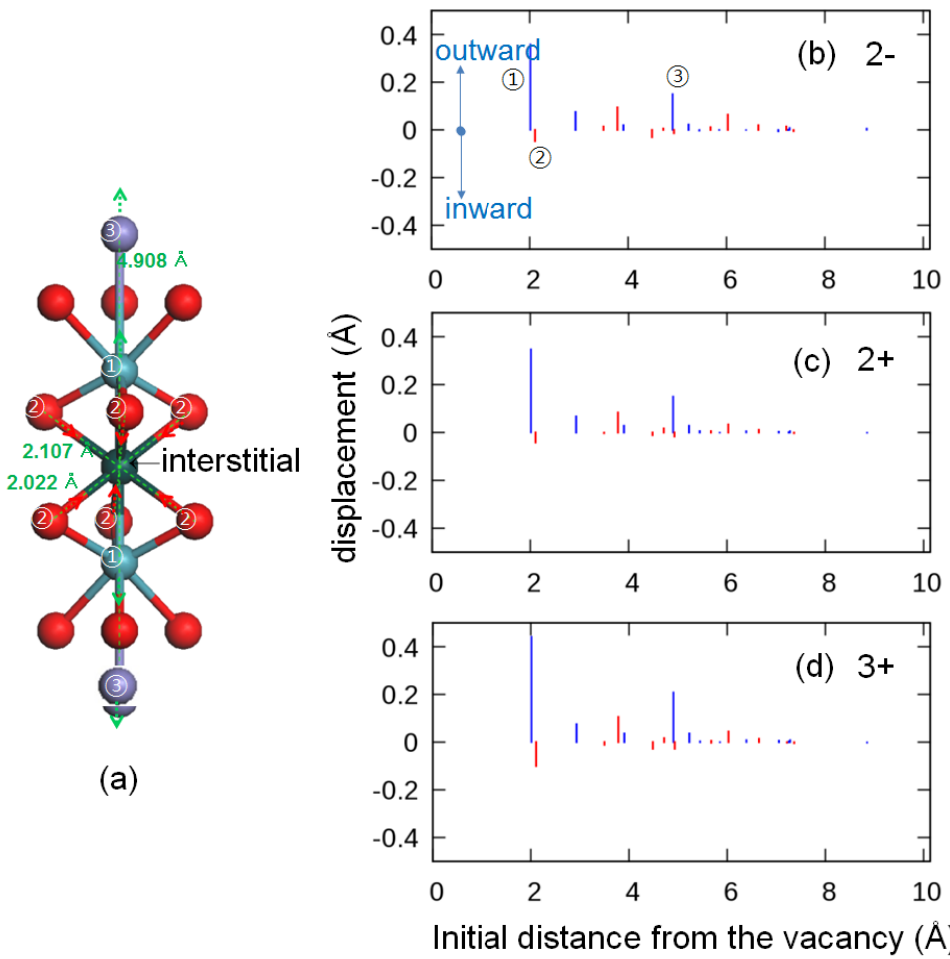

Fig. 16 (a) and (b),(c),(d) display relaxation patterns and ionic displacements in system with interstitial Fe depending on the distance from the defect. (b) is for Fe_I^{2-}, (c) is for Fe_I^{2+}, and (d) is for Fe_I^{3+}

4.4.2. Fe_I : electronic structure

The electronic structure of interstitial Fe making spin configuration of $\uparrow\downarrow(\downarrow)\downarrow\uparrow$ is shown in Fig. 17 and that making $\uparrow\downarrow(\uparrow)\downarrow\uparrow$ is shown in Fig. 18. For most charged state, former one is stable than latter, but 3+ charged state is only stably found in latter case. When the formal one is introduced, minority spin states of Fe ions on the next floor ($Fe_{\downarrow}^{1F}$) and the second next floor ($Fe_{\uparrow}^{2F}$) are induced inside the band gap and occupied or not depending on the Fermi level, which are originally above the CBM and unoccupied. If the β, γ levels are occupied and α level is unoccupied, it is considered as neutral state. On the other hand, when Fe_I with positive spin ($Fe_{\uparrow}^{int}$) is introduced between the Fe ions with negative spin ($Fe_{\downarrow}^{1F}$), not only the minority spin states of Fe $_{\downarrow}^{1F}$ are induced in the gap as same as the former case, but also the minority spin states of neighboring Fe ions on the same layer ($Fe_{\uparrow}^{p}$) are induced in the gap. In this case, 3+ charged state is stably formed.

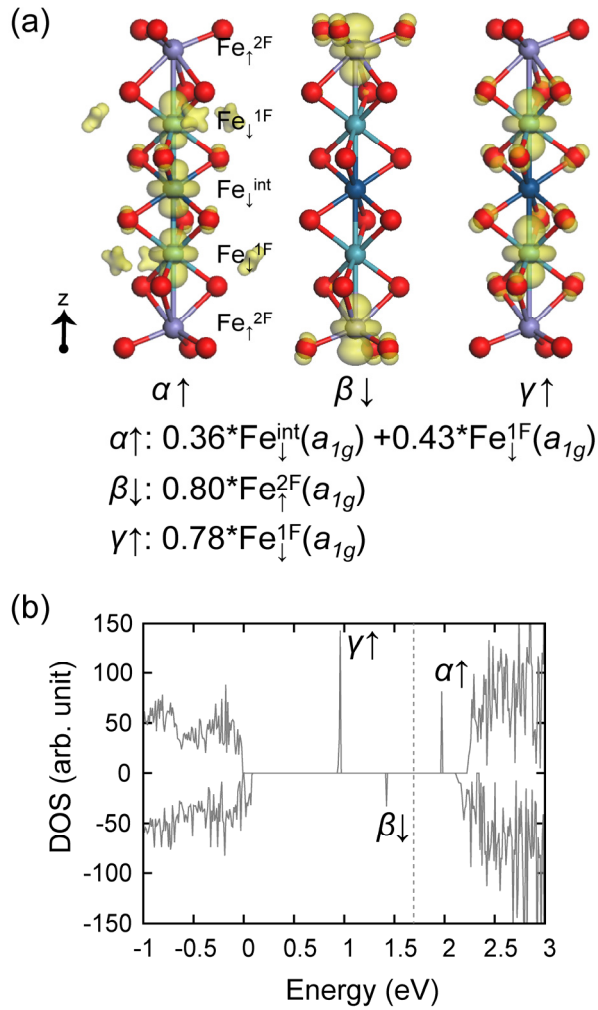

Fig. 17 (a) Partial charge distribution of defect states, and (b) DOS of the defective system with $Fe_{\downarrow}^{int}$.

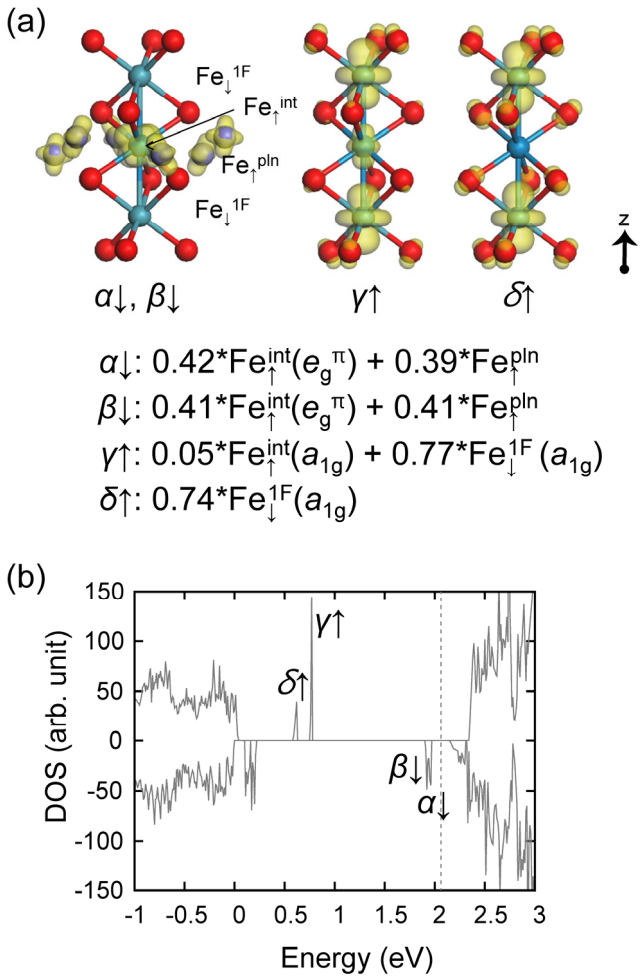

Fig. 18 (a) Partial charge distribution of defect states, and (b) DOS of the defective system with $Fe_{\uparrow}^{int}$.

4.5. Electron small polaron

Electron carrier generally can be delocalized into the conduction band, or localized in a self-induced distortion of its surroundings. In the latter case, when the distortion is localized to a region that is less than the lattice constant, it is called small polaron. [13] Substantial empirical modeling studies explain the conductivity behavior using the small polaron model, where the electron exists as a localized particle at Fe ion in the Fe_2O_3 lattice.[14-18] We obtained negative self-trap energy value E_{ST} = -0.57 eV which implies the self-trap system of electron polaron. Electron undergoes smaller relaxations than the V_{Fe} with the same pattern. Electron polaron and V_{Fe} are same in a sense that effective positive charge at Fe site is decreased (or disappeared). Electron polaron is localized at Fe $d(t_{2g})$ orbital which is the minority spin state and also has perturbed states resembling VBM around the polaron site.

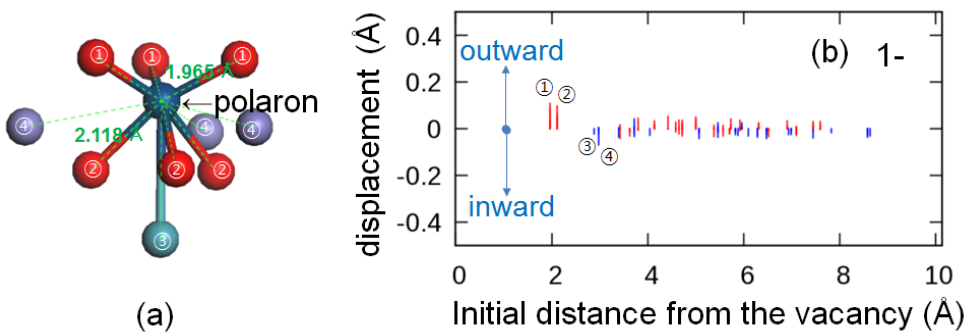

Fig. 19 (a) is relaxation patterns in system with electron polaron, (b) shows ionic displacements in the system with respect to the distance from the polaron site.

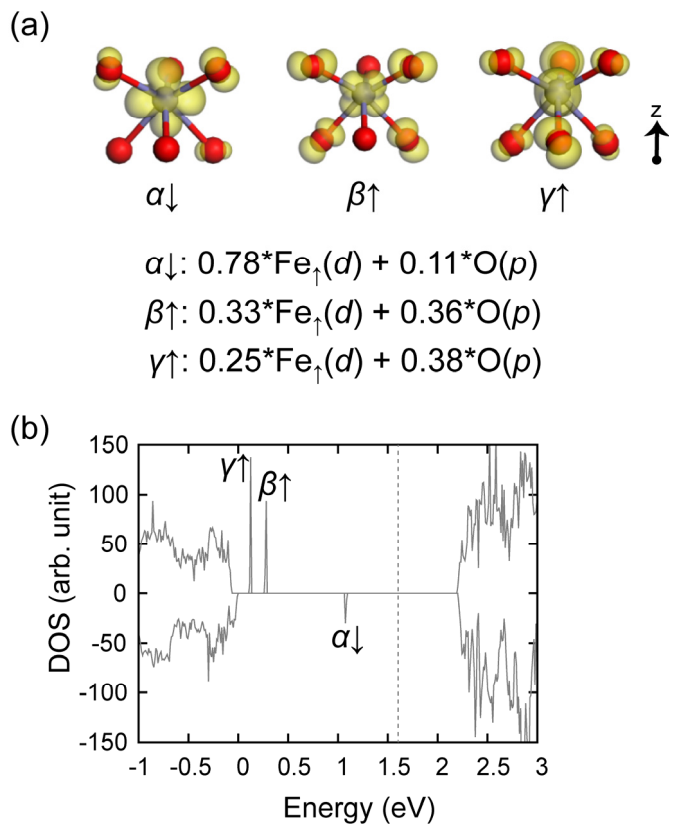

Fig. 20 (a) Partial charge distribution of polaron states, and (b) DOS of the system with electron polaron.

4.6. Formation energies

In addition to the properties of defects when they exist solely in the crystal, energetics of the defect formation also have to be studied. In the supercell formalism, the formation energy of a defect with charge state q is defined as the following form.

$$\Delta E_f(\text{defect},q) = E(\text{defect},q) - E(\text{perfect}) + n_{\text{O}}\mu_{\text{O}} + n_{\text{Fe}}\mu_{\text{Fe}} + q(\varepsilon_F + E_{\text{VBM}}), \quad (6)$$

where E(defect,q), E(perfect), n_i and μ_{i} are the total energy of the defective supercell with charge state q, and corresponding clean supercell energy, the number of atomic species i that is removed or added, and the chemical potential of the species, respectively. The last term of electron chemical potential is Fermi energy of the system, where the valance-band maximum E_{VBM} is set to zero for ε_{F}.

The material's growth conditions or the equilibrium conditions are reflected in the chemical potentials of atoms removed or added when the defect is formed. Metal-rich and oxygen-rich conditions are considered as the two extreme conditions of the defective Fe_2O_3 system. Chapter 4.6.2 will present the details of this issue.

4.6.1. Correction of size effect

Since we utilize the periodic boundary condition for DFT calculations, the calculated formation energies are introducing an error that converges with supercell size, so we have to conduct appropriate correction to mimic isolated defect by finite supercell calculation.

4.6.1.1. Potential alignment correction[20]

When defect is formed in periodic supercell, the average electrostatic potential within the cell will diverge. In order to prevent this problem, average electrostatic potential is set to zero within the pseudo potential reciprocal space formalism, i. e:

$$V_{el}(G) = \frac{8\pi\rho(G)}{G^2} = 0\Big|_{G=0}. \qquad (7)$$

Such treatment is not resulting on the change of total energy of the system but on eigenvalues, thus energy of the defective cell with charge q rises by $q^{*}\Delta V_{\mathrm{PA}}$, where ΔV_{PA} means the constant potential shift called potential alignment (PA). For determining ΔV_{PA}, we used the average potential at oxygen core site as the reference.

4.6.1.2. Makov-Payne correction

Adjustment of the G = 0 term is effectively described as introducing a compensating background charge called jellium background. This results in spurious interactions between the background charge and the periodic charged defects, which cause the cell size dependence of

defect formation energies. Makov and Payne proposed the correction energy terms assuming a molecule-like charged species in cubic supercells, and it is defined as

$$E_{corr}^{MP} = \frac{q^2\alpha}{2\varepsilon L} + \frac{2\pi qQ}{3\varepsilon L^3} + O(L^{-5}) = E_{MP1} + E_{MP2}, \quad (8)$$

where q, ε, α, and Q are defect charge, static dielectric constant, Madelung constant, and second moment of defect charge distribution, respectively. E_{MP1} represent the monopole-monopole interaction between repeated localized point charges within jellium background, and E_{MP2} is monopole-quadrupole interaction. We applied correction over only E_{MP1} term when we call MP correction.

4.6.1.3. Reference value from extrapolation scheme

Figure 21 displays the variations of the calculated formation energy with different cell size. L is the cubic root of supercell volume. We also marked the number of atoms within each supercell. Here we show the case of V_O^{2+}, and as Makov and Payne described the values are showing the dependence of

$$\Delta E_f = a + \frac{b}{L} + \frac{c}{L^3} \quad (L = V^{1/3}). \quad (9)$$

MPPA indicates formation energy corrected by both MP and PA. We also applied Lany-Zunger (LZ) scheme where the E_{MP1} is scaled by a factor of about 0.65.[20] Each data set corresponding to different correction scheme is fitted by Eq.(9) using data of supercells with 120, 180, 270, 360 and 640 atoms. We did not include the result of cell with

80 atoms for fitting because large error is expected due to small cell size. It is noted that the formation energy from each correction scheme converge to the certain value at the limit of infinite cell size ($L^{-1} \rightarrow 0$) as shown in Fig. 21, and therefore the value can be regarded as the reference for formation energy of isolated defect. We found that the calculated formation energy using supercell with 120 atoms is comparable to the reference value after MPPA correction. For that reason, following discussion on the formation energy of intrinsic defect will be proceeded using 120 atoms supercell considering MPPA method.

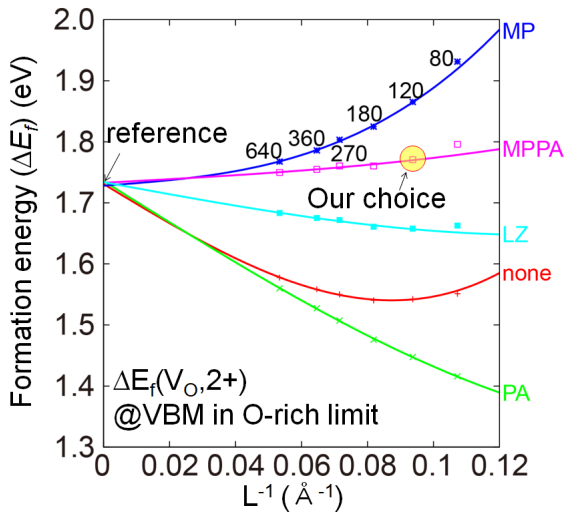

Fig. 21 Reference for correction[21]. The figure shows convergence of defect formation energies of V_O^{2+} with respect to the supercell size with 80, 120, 180, 270, 360, and 640 atoms. The x-axis is inverse cubic root of volume. MP, MPPA, LZ, and PA indicates data corrected by Makov-Payne method, MP with potential alignment correction (PA), Lany-Zunger method, and only PA, respectively. 'None' means the data with no correction.

4.6.2. Charge transition level

As mentioned in chapter 4.6, the formation energies of defects are written in the form depends on the atomic chemical potential μ_i and Fermi level ε_F. For a kind of defect, atomic chemical potential term is constant even if it is not determined yet, while the Fermi level term affects formation energy by factors of q which are variant from different charged states. So, the most stable charged state changes with respect to ε_F. The figure that shows the most stable charged states of each defect and then the charge transition levels is called charge transition level diagram. The diagram is shown in Fig. 22, where the atomic chemical potential is determined as two limit conditions as follows.

The range of μ_O is restricted to

$$\mu_O^{\text{metal-rich}} < \mu_O < \mu_O^{\text{oxygen-rich}}, \tag{10}$$

where the right hand side is the limit when Fe_2O_3 is in equilibrium with oxygen gas, while the left hand side is the limit when Fe_2O_3 is in equilibrium with magnetite (Fe_3O_4).

When Fe_2O_3 is in equilibrium with oxygen gas,

$$\mu_{O,T} = \frac{1}{2}\mu_{O_2,T,p}, \tag{11}$$

and

$$\frac{1}{2}\mu_{O_2,T,p} = \frac{1}{2}\mu_{O_2,0K,p^\circ} + \frac{1}{2}\Delta\mu_{O_2,T,p^\circ} + \frac{1}{2}kT\ln\left(\frac{p}{p^\circ}\right), \tag{12}$$

thus

$$\mu_{O,T} \le \frac{1}{2}\mu_{O_2,0K,p^\circ}, \tag{13}$$

From this, we define oxygen chemical potential at oxygen-rich condition and obtain the value from first-principles calculation:

$$\mu_O^{\text{oxygen-rich}} = \frac{1}{2}\mu_{O_2,0K,p^\circ} = \frac{1}{2}E_{O_2}^{\text{total}} = -4.933 \text{ eV}. \tag{14}$$

On the other hand, when Fe_2O_3 and Fe_3O_4 is in equilibrium,

$$\mu_{O,T} = 3\mu_{Fe_2O_3,T} - 2\mu_{Fe_3O_4,T}, \tag{15}$$

and

$$\begin{aligned} &3\mu_{Fe_2O_3,T} - 2\mu_{Fe_3O_4,T} = \\ &3\left\{\mu^\circ_{Fe_2O_3,298K} + \Delta\mu_{Fe_2O_3,T}\right\} - 2\left\{\mu^\circ_{Fe_3O_4,298K} + \Delta\mu_{Fe_3O_4,T}\right\} = \\ &3\mu^\circ_{Fe_2O_3,0K} - 2\mu^\circ_{Fe_3O_4,0K} + 3\Delta\mu^\circ_{Fe_2O_3,T} - 2\Delta\mu^\circ_{Fe_3O_4,T} \end{aligned}, \tag{16}$$

where the following condition is valid according to the thermodynamic table:

$$3\Delta\mu^\circ_{Fe_2O_3,T} - 2\Delta\mu^\circ_{Fe_3O_4,T} \ge 0, \tag{17}$$

and therefore in equilibrium with Fe_3O_4:

$$3\mu^\circ_{Fe_2O_3,0K} - 2\mu^\circ_{Fe_3O_4,0K} \le \mu_{O,T}. \tag{18}$$

From the above, we define oxygen chemical potential at metal-rich condition by:

$$\mu_O^{\text{metal-rich}} = 3\mu^\circ_{Fe_2O_3,0K} - 2\mu^\circ_{Fe_3O_4,0K}. \tag{19}$$

In calculation formalism, however, a problem exists when we try to determine the oxygen chemical potential at metal-rich condition, which is related to the difference of practical effective U parameter between

Fe_3O_4 and Fe_2O_3 systems in GGA+U framework. For Fe_3O_4 systems, people use U_{eff} = 3.61 eV[19], and for Fe_2O_3 systems, they use U_{eff} = 4.3 eV[9]. Because the energies with different computational settings cannot be compared, we calculated the oxygen chemical potential at metal-rich condition with both of U_{eff} values stated above. In the case of U_{eff} = 3.61 eV, the value was -7.20 eV, while in the case of U_{eff} = 4.3 eV, the value was calculated as -6.99 eV. These values are the same as -2.07 eV, -2.28 eV respectively when we set the reference to the half of the chemical potential of oxygen gas (-4.933 eV).

Experimentally, the value can be calculated from the heat of formation of Fe_2O_3 and Fe_3O_4:

$$2\mathrm{Fe}(s)+\frac{3}{2}\mathrm{O}_2(g)\rightarrow \mathrm{Fe}_2\mathrm{O}_3(s,\ \text{hematite}),\qquad \Delta G^{\circ}_{298K}=\text{-7.680 eV};$$

$$3\mathrm{Fe}(s)+2\mathrm{O}_2(g)\rightarrow \mathrm{Fe}_3\mathrm{O}_4(s,\ \text{magnetite}),\qquad \Delta G^{\circ}_{298K}=\text{-10.509 eV}. \tag{20}$$

Chemical potential is defined as the slope of the free energy of the system with respect to a change in the number of moles of corresponding species:

$$\mu^{\circ}_{\mathrm{Fe_2O_3},298\mathrm{K}}-2\mu^{\circ}_{\mathrm{Fe_2O_3},298\mathrm{K}}-\frac{3}{2}\mu^{\circ}_{\mathrm{O_2},298\mathrm{K}}=\text{-7.680 eV},$$

$$\mu^{\circ}_{\mathrm{Fe_3O_4},298K}-3\mu^{\circ}_{\mathrm{Fe},298K}-2\mu^{\circ}_{\mathrm{O_2},298K}=\text{-10.509 eV}. \tag{21}$$

From the Eq.(21) the following is calculated,

$$
\begin{aligned}
&3\left[\mu^{\circ}_{Fe_2O_3,298K}-2\mu^{\circ}_{Fe_2O_3,298K}-\frac{3}{2}\mu^{\circ}_{O_2,298K}\right]\\
&-2\left[\mu^{\circ}_{Fe_3O_4,298K}-3\mu^{\circ}_{Fe,298K}-2\mu^{\circ}_{O_2,298K}\right]\\
&=3\mu^{\circ}_{Fe_2O_3,298K}-2\mu^{\circ}_{Fe_3O_4,298K}-\frac{1}{2}\mu^{\circ}_{O_2,298K}=\text{-2.021 eV},
\end{aligned}
\tag{22}
$$

The oxygen chemical potential at metal-rich condition is expressed in the term of oxygen gas energy. Oxygen gas energy can be treated with calculated value as same as in the Eq.(14), and other terms are replaced with experimental values according to the thermodynamic tables:

$$
\begin{aligned}
\mu_O^{\text{metal-rich}} &= 3\mu^{\circ}_{Fe_2O_3,0K}-2\mu^{\circ}_{Fe_3O_4,0K}\\
&=\left(3\mu^{\circ}_{Fe_2O_3,298K}-2\mu^{\circ}_{Fe_3O_4,298K}\right)-\left(3\Delta\mu^{\circ}_{Fe_2O_3,298K}-2\Delta\mu^{\circ}_{Fe_3O_4,298K}\right)\\
&=\left(\frac{1}{2}\mu^{\circ}_{O_2,298K}-2.021\text{ eV}\right)-\left(3\Delta\mu^{\circ}_{Fe_2O_3,298K}-2\Delta\mu^{\circ}_{Fe_3O_4,298K}\right)\\
&=\left(\frac{1}{2}E^{\text{total}}_{O_2}+\frac{1}{2}\Delta\mu^{\circ}_{O_2,298K}-2.021\text{ eV}\right)-0.056\text{ eV}=-7.290\text{ eV}.
\end{aligned}
\tag{23}
$$

This value is comparable to the fully computational values (-7.20 eV with U_{eff} = 3.61 eV, -6.99 eV with U_{eff} = 4.3 eV), so we used the value in Eq.(23) to get rid of the issue of determining U_{eff}. Conclusively, the range of the oxygen chemical potential is determined as the following, replacing Eq.(10):

$$
-7.290\text{ eV} < \mu_O < -4.933\text{ eV}. \tag{24}
$$

Using these values, we show charge transition diagrams at metal-rich condition and oxygen-rich condition in Fig. 22.

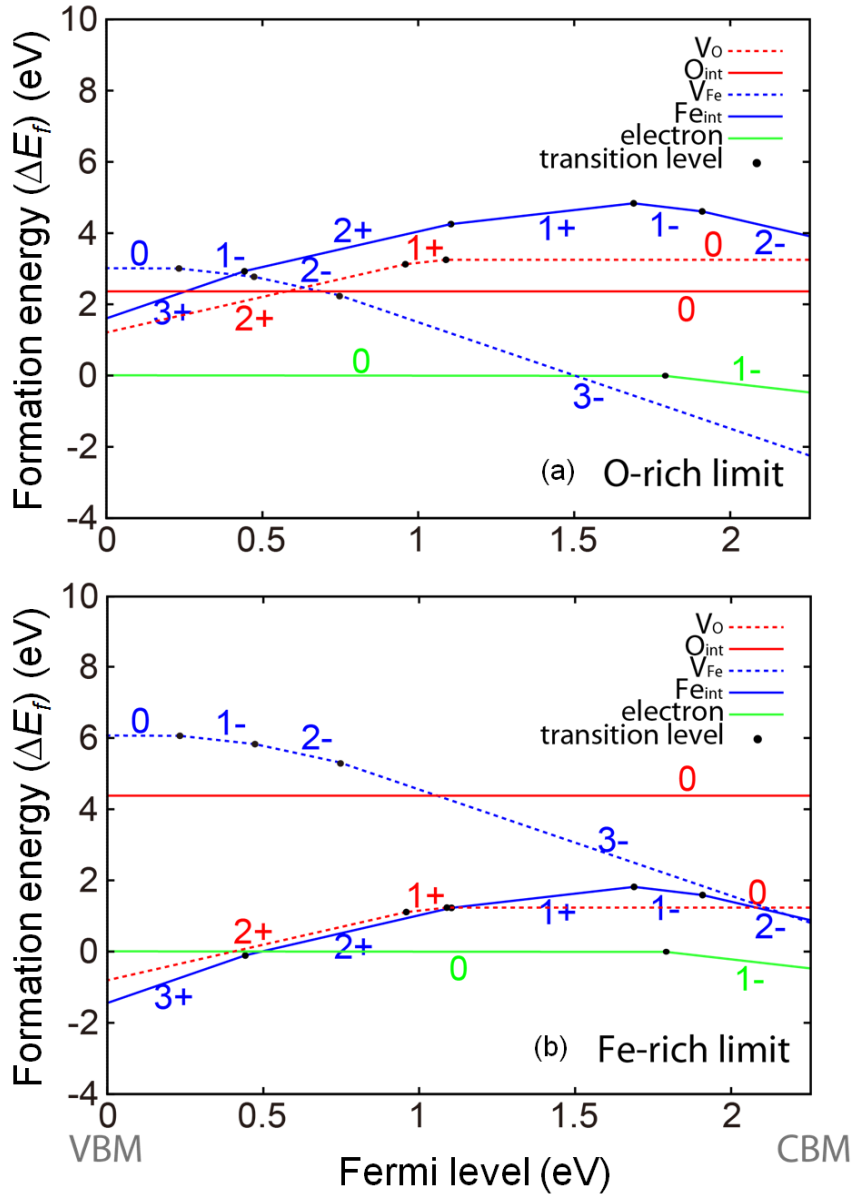

Fig. 22 Charge transition level diagrams as a function of Fermi level in (a) O-rich and (b) Fe-rich limits. The formation energies of V_O (red dashed), O_I (red), V_{Fe} (blue dashed), Fe_I (blue), and electron polaron (green lines) are presented. and black dots indicate transition levels.

4.7. Concentration of defects

Concentrations of each kind of defect with charge q are written as

$$\frac{[\mathrm{D}_X(q)]}{\mathrm{n_X}} = \frac{\exp(-\Delta E_f\{\mathrm{D}_X(q)\}/k_BT)}{1+\sum_{q'}\exp(-\Delta E_f\{\mathrm{D}_X(q')\}/k_BT)}, \quad (25)$$

where $[D_X(q)]$, n_X, $\Delta E_f\{D_X(q)\}$, and k_BT are the concentration of defect D_X with charge q, the concentration of possible lattice sites for the defect, defect formation energy, and Boltzmann factor, respectively. q' represents possible charge states of the defects.

Because, $\sum_{q'}\exp(-\Delta E_f\{\mathrm{D}_X(q')\}/k_BT)$ is much smaller than 1, therefore Eq.(25) can be approximated as

$$\frac{[\mathrm{D}_X(q)]}{\mathrm{n_X}} \approx \exp(-\Delta E_f\{\mathrm{D}_X(q)\}/k_BT). \quad (26)$$

We evaluated the concentration of each defect using Eq.(26). In addition, the electron polaron is considered as a defect which is localized at Fe site. In contrast to the electron polaron concentration, hole concentration is evaluated considering Fermi-Dirac statistics and density of states of valence band assuming the delocalization of the wave function of hole:

$$p = \int_{-\infty}^{E_{VBM}} D(\varepsilon) f_h d\varepsilon \cong \sum_{i=occupied} f_h(\varepsilon_i, \varepsilon_F). \quad (27)$$

We approximate the integration of given function as the summation of finite values for the convenience of calculation. For calculation, we sampled $30\times30\times30$ k-point mesh within the Brillouin zone, and performed the summation over all k-points and occupied bands:

$$\sum_{n=occupied}\sum_{k} w_k f_h(\varepsilon_i, \varepsilon_F), \tag{28}$$

where w_k is the weight factor of the k-point, and f_h is the Fermi-Dirac distribution of hole:

$$f_h(\varepsilon_i, \varepsilon_F) = \frac{e^{(\varepsilon_i - \varepsilon_F)/k_B T}}{e^{(\varepsilon_i - \varepsilon_F)/k_B T} + 1}. \tag{29}$$

Generally speaking, the formation energies of charged defects are affected by Fermi level. Therefore, we have to obtain intrinsic Fermi level satisfying the charge neutrality condition. For charge neutrality, the total sum of charges has to be zero in equilibrium:

$$\sum_{X}\sum_{q'} q' \cdot [\mathrm{D}_X(q')] - n + p = 0, \tag{30}$$

where n, p are concentrations of electronic polaron and hole. There is an energy level within the band gap which agrees with Eq.(30). Fermi level is obtained using Shockley diagram which displays the total density of positive and negative charges logarithmically as a function of Fermi level. For example, Fig. 23 and 24 show the Shockley diagrams at the usual preparation temperature of 1273K and at room temperature (R.T. = 300K), respectively. The lines of total negative and positive charge which include charged defects, electron polaron and hole meet at the intrinsic Fermi level to satisfy the charge neutrality condition. In this way, intrinsic Fermi level at various temperatures and atomic chemical potentials can be determined by charge neutrality condition. Therefore, the density of intrinsic point defect can be calculated at a given thermodynamic conditions.

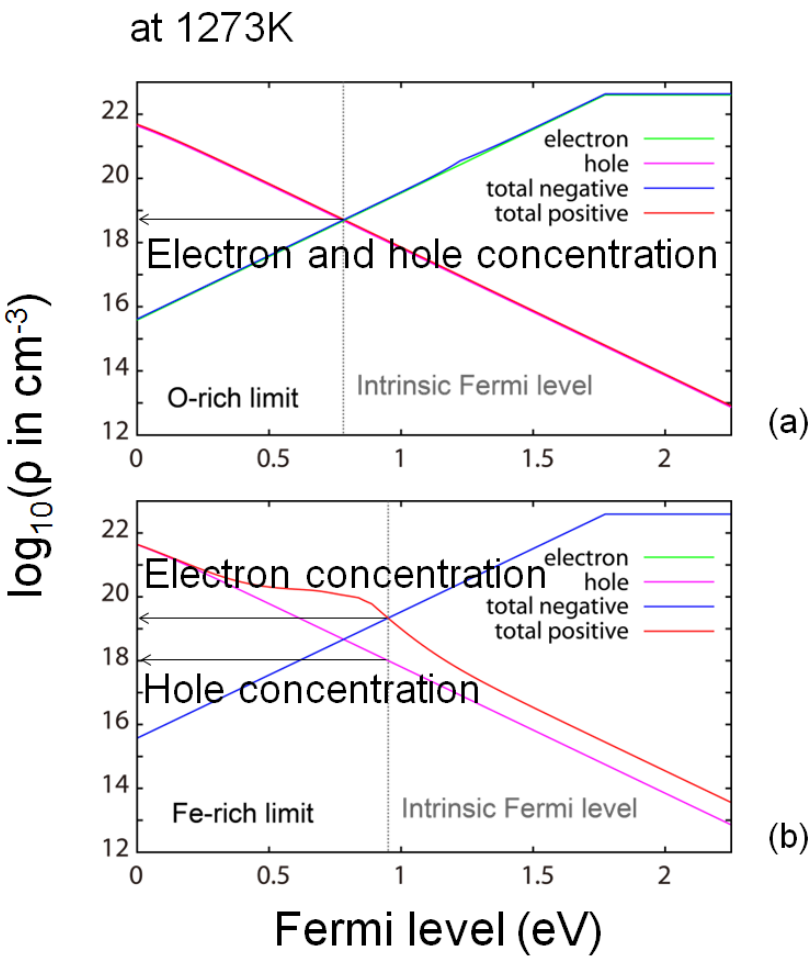

Fig. 23 Shockley diagrams show concentrations of charged species as a function of Fermi level at 1273K in (a) O-rich and (b) Fe-rich conditions. Concentrations of electron polaron (green), hole (magenta), total negative (blue) and total positive charges (red line) are presented.

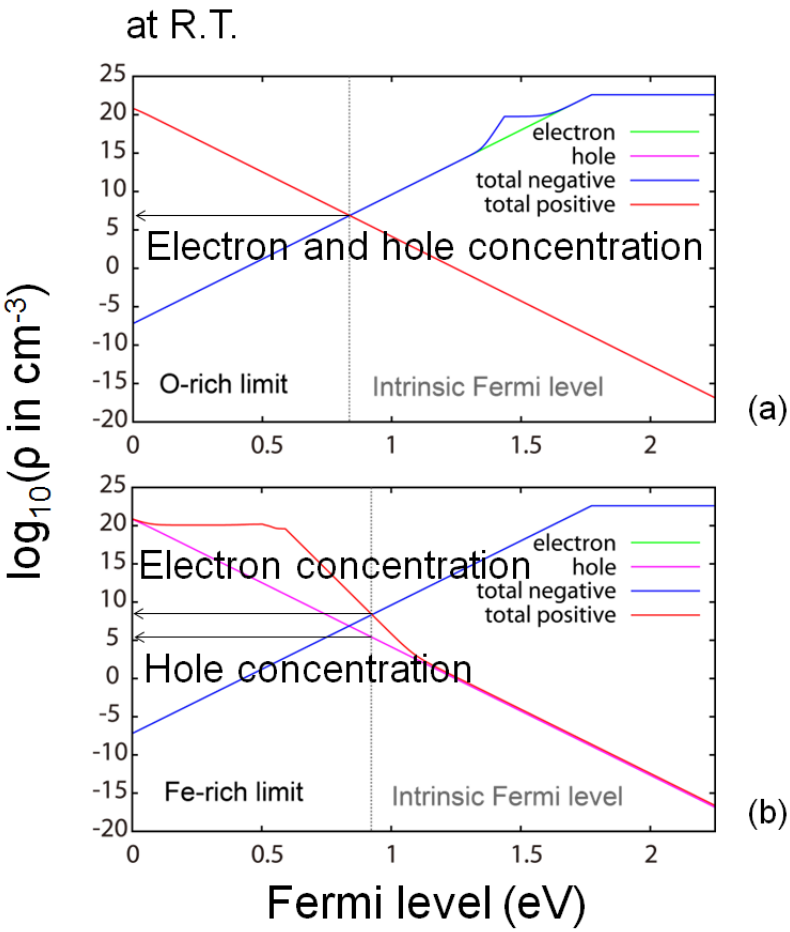

Fig. 24 Shockley diagrams show concentrations of charged species as a function of Fermi level at 300K in (a) O-rich and (b) Fe-rich conditions.

4.8. Equilibrium condition

We plot the variations of Fermi level and densities of major defects with respect to the oxygen chemical potential in equilibrium at 1273K in Fig. 25 and at R.T. in Fig. 26 (We call it Kröger-Vink diagram or Brower diagram). In addition, densities of major defects are displayed as a function of temperature in Fig. 27. Using calculated defect concentrations, composition ratio depending on oxygen chemical potential can be derived as in Fig. 28a. Salmon[22] has reported that the Fe_2O_3 fabricated in air condition exhibit the oxygen deficiency. and also stated that for Fe_2O_3 in equilibrium with Fe_3O_4 the value of x in Fe_2O_{3-x} ranges from 0.0015 at 1000℃ to 0.01 at 1500℃. It is fairly comparable to our calculation value, 0.0013 at 1000℃ (1273K) in Fig. 28a, which validates our defect concentrations calculations.

In addition, practical range of oxygen chemical potential in equilibrium condition can be estimated by the following thermodynamic relations:

$$\begin{aligned} & 3\mu_{\mathrm{Fe_2O_3},T} - 2\mu_{\mathrm{Fe_3O_4},T} < \mu_{\mathrm{O},T,p} < \frac{1}{2}\mu_{\mathrm{O_2},T,p} \ , \\ & \mu_{\mathrm{O}}^{\text{metal-rich}} + 3\Delta\mu^{\circ}_{\mathrm{Fe_2O_3},T} - 2\Delta\mu^{\circ}_{\mathrm{Fe_3O_4},T} < \mu_{\mathrm{O},T,p} \\ & \qquad < \mu_{\mathrm{O}}^{\text{oxygen-rich}} + \frac{1}{2}\Delta\mu_{\mathrm{O_2},T,p^{\circ}} + \frac{1}{2}kT\ln(\frac{p}{p^{\circ}}) . \end{aligned} \tag{31}$$

The estimated oxygen chemical potential values using thermodynamic tables are shown in Fig. 28b. Red and cyan lines show the practical boundary of oxygen chemical potential at varying temperature, and points are oxygen chemical potentials in equilibrium with oxygen gas of partial pressure p_{O2} at temperature T. Stoichiometry condition is

presented as black line; shaded region below the line is oxygen deficient region. Hematite decomposes to magnetite at 1653K in air condition as reported by Gardner *et al.*[1]

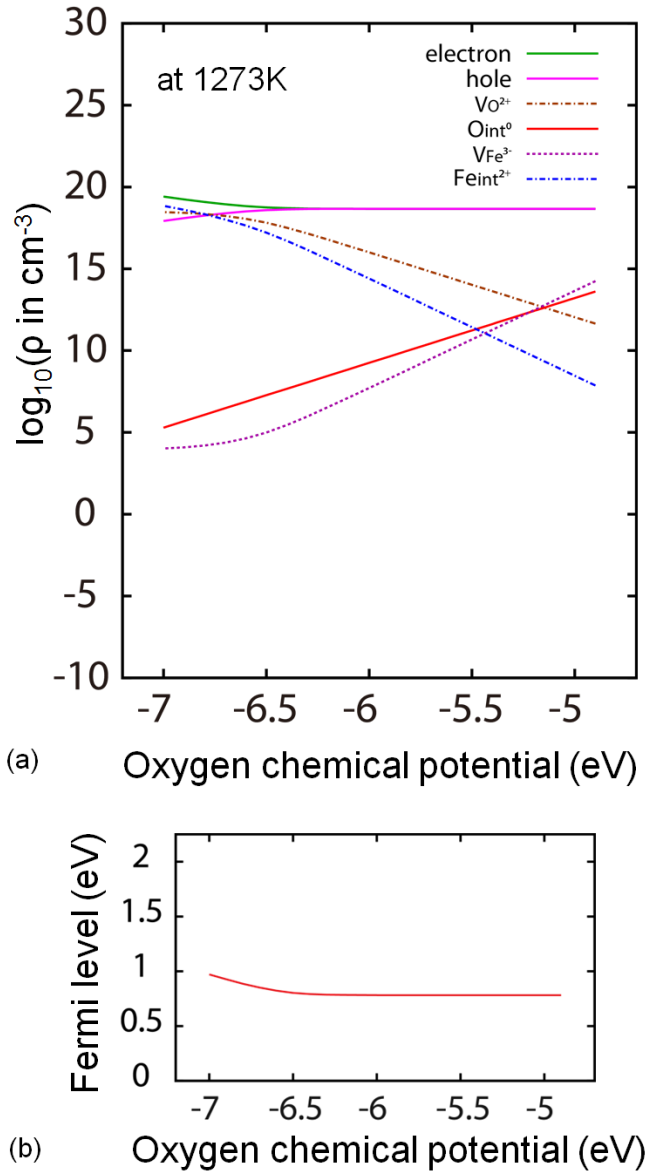

Fig. 25 (a) Kröger-Vink diagram (Brower diagram) for equilibrium condition at 1273K, and (b) corresponding Fermi level are shown.

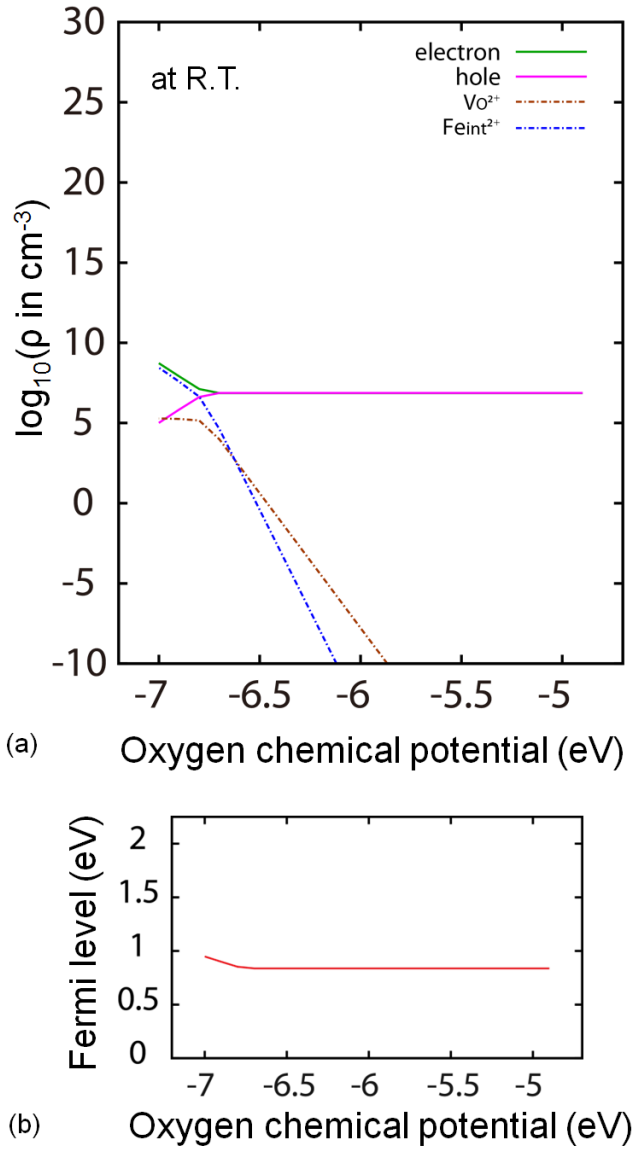

Fig 26 (a) Kröger-Vink diagram (Brower diagram) for equilibrium condition at 300K, and (b) corresponding Fermi level are shown.

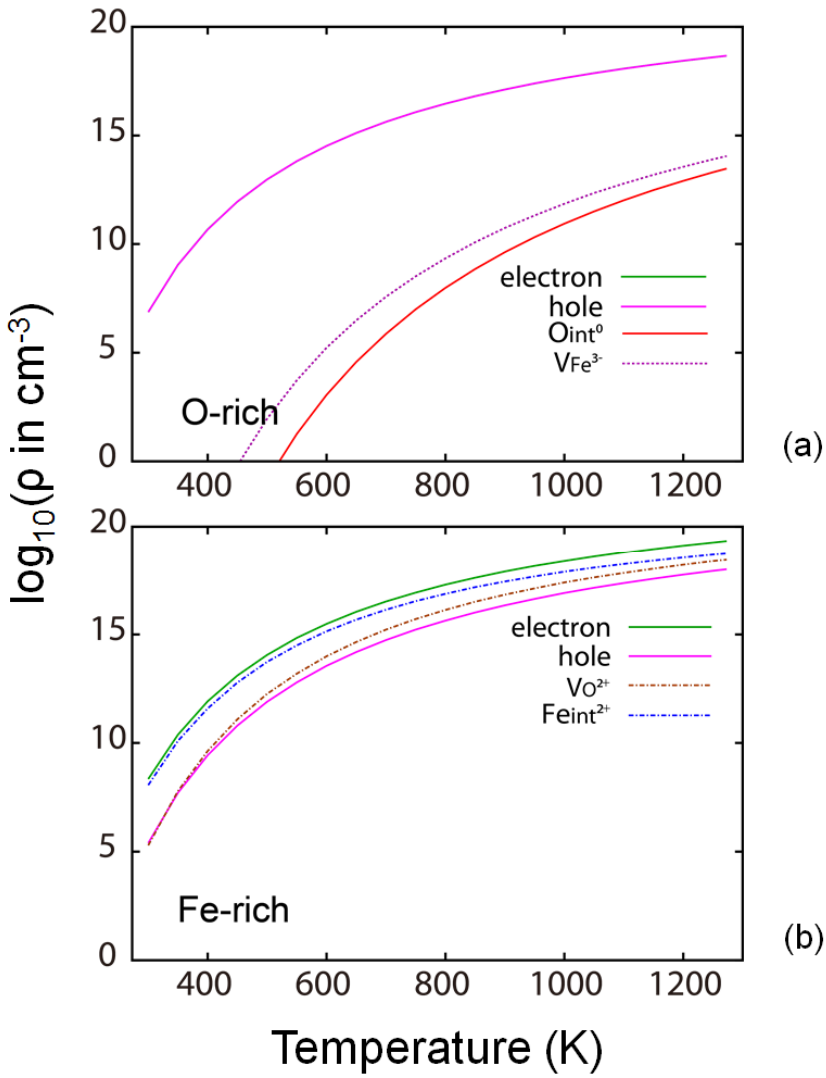

Fig. 27 Concentrations of dominant species as a function of the equilibrium temperature in (a) O-rich and (b) Fe-rich conditions

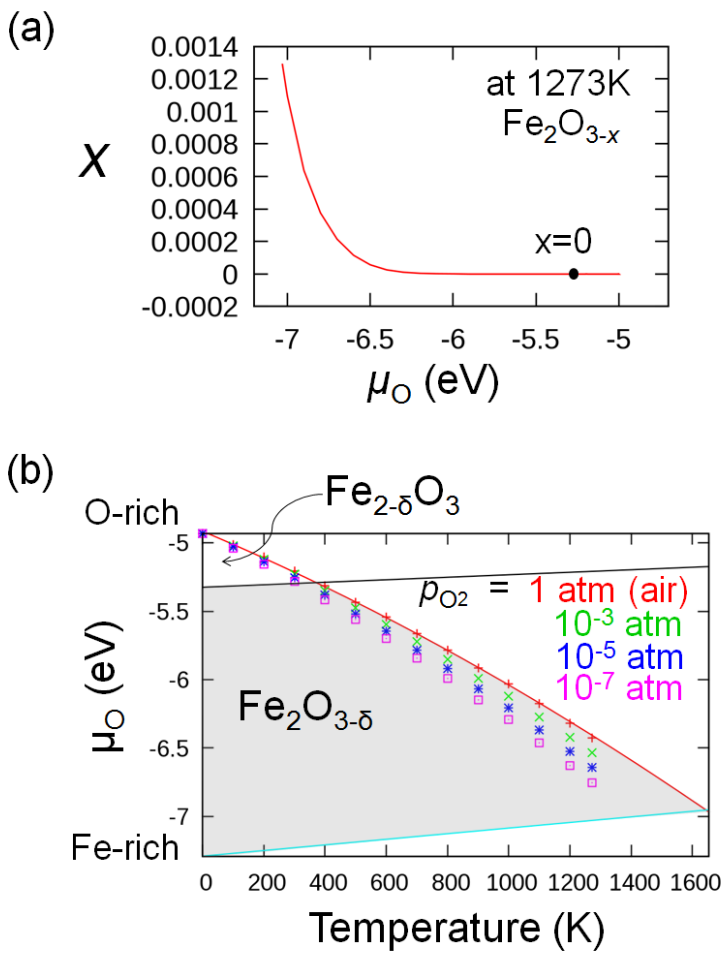

Fig. 28 (a) Fe_2O_{3-x} composition at 1273K with respect to the oxygen chemical potential. (b) practical oxygen chemical potentials at various temperatures and oxygen partial pressure.

4.9. Quenched condition

Although we dealt with the defect densities in thermal equilibrium, in the common operating condition it is hard to reach thermal equilibrium. In other words, the device made of Fe_2O_3 fabricated at relatively high temperature, which means the equilibrium may be achieved. In the operating condition, the device is, however, typically used at room temperature (R.T.). In that case, we assume that the portions of each defect are changed, even though the total concentrations of each defect are not varied. Because the ions are immobile due to its large mass while the holes or electron polarons are easy to move. This situation is similar to the case of extrinsic doping, and we call it 'defect quenching'. To find out the ratio of charged defect concentration to total concentration of the given defect, we use the following formula:

$$\frac{[\mathrm{D}_X(q)]}{\sum_{q'}[\mathrm{D}_X(q')]} = \frac{\exp(-\Delta E_f\{\mathrm{D}_X(q)\}/k_BT)}{\sum_{q'}\exp(-\Delta E_f\{\mathrm{D}_X(q')\}/k_BT)}, \tag{32}$$

where denominator of the left hand side term is fixed to that of fabrication condition, and then $[D_X(q)]$ is determined from right hand side of the equation. In the right side of equation, the numerator and the denominator cancel each other as for constant terms inside the exponential functions, so the only need to know is the new temperature condition and the difference of the formation energies of each charged state. As a result, new intrinsic Fermi level is built that agrees the charge neutrality condition with the changed densities.

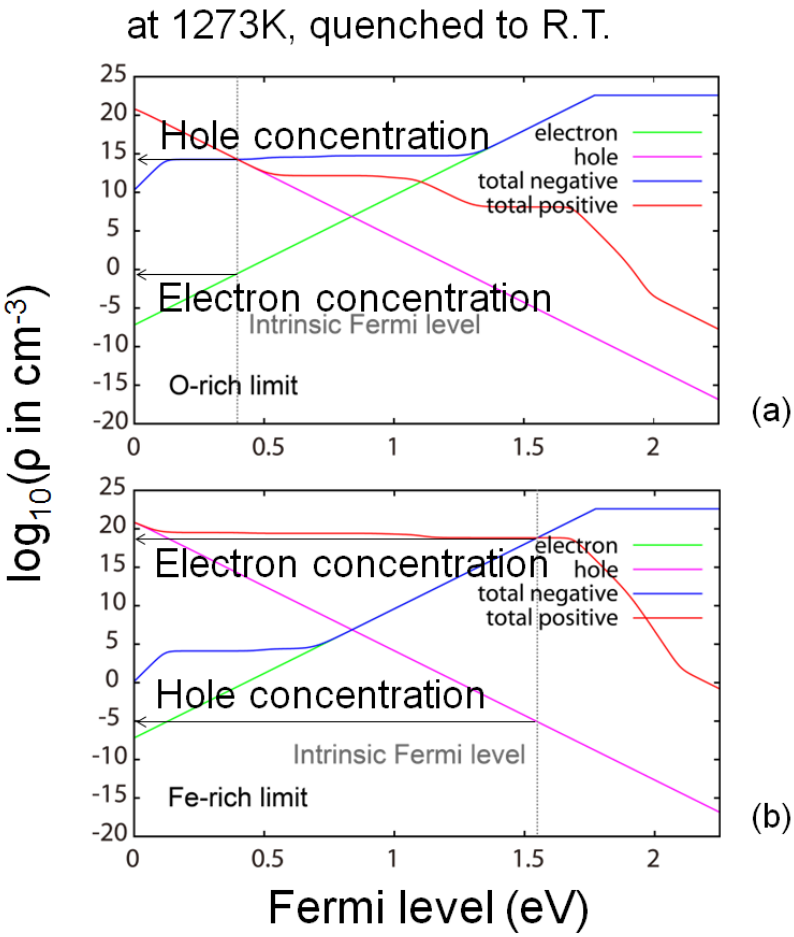

Fig. 29 Shockley diagrams show equilibrium concentrations of charged species in the system that equilibrated at 1273K and quenched to R.T. (a) is of O-rich and (b) is of Fe-rich conditions.

The result is represented in Fig. 29. In Fig. 29b the uppermost lines in one color follow the line in the same color in Fig. 25b which is for equilibrium at 1273K. However, the electronic equilibrium concentrations of hole and electron polaron are changed to lower values of at R.T.. Therefore, Fermi level is determined by the concentrations of dominant charged defects instead of those of hole and electron polaron. In contrast to the 300K equilibrium case, the variations of defect concentrations which depend on the atomic chemical potentials lead to change of Fermi energy. The changing Fermi level gives rise to transitions between various charged states of each defect. It is notable that the neutral V_O is most stable in comparison with charged V_O within the wide range of μ_O, which indicates that the oxygen vacancy works as a deep donor leading them to seldom contribute to *n*-type conductivity. In Fig. 26, we can divide the regions with respect of the dominant charged species in equilibrium including defects, hole, and electron polaron. In region i, concentration of singly charged Fe_I is in equilibrium with electron concentration, In region ii, singly charged V_O and electron are in equilibrium. In region iii, charged V_O and V_{Fe} are in equilibrium and neutral O_I is also dominant, which makes in this region Schottky defects and anti-Frenkel defects balance the charge neutrality and also the stoichiometry condition. Finally in region iv, singly charged V_{Fe} is dominant which gives rise to *p*-type character.

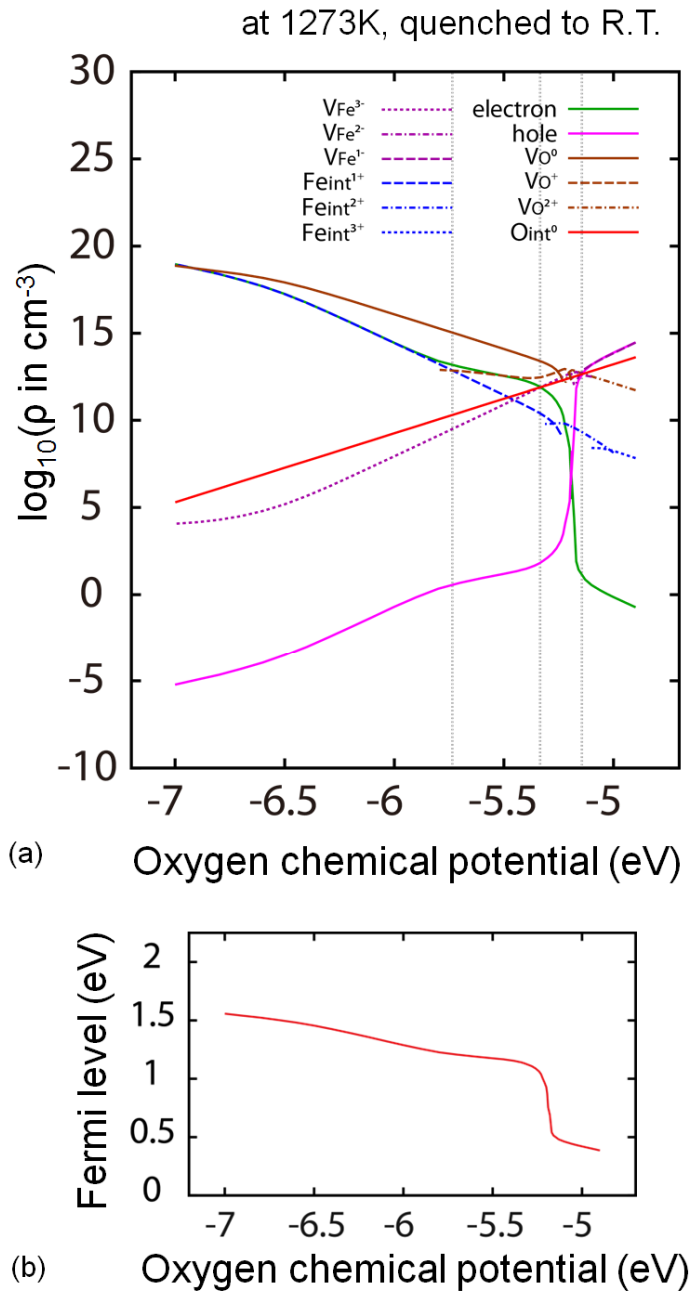

Fig. 30 (a) Kröger-Vink diagram (Brower diagram) of system that equilibrated at 1273K and quenched to R.T.,, and (b) corresponding Fermi level

CHAPTER 5

Conclusion

We studied the intrinsic point defects within GGA+U formalism. Overall high formation energies of defects result in small deviation from stoichiometry at low temperature. In this case, electronic equilibrium is more important to carrier densities than defect controlled behavior. However, when Fe_2O_3 is fabricated at high temperature, defects are easily formed by temperature effect. In this condition, even if the material is quenched to room temperature, donor or acceptor centers are remained at high concentrations while the electronic equilibrium concentrations of hole and electron polaron are lowered to those at R.T. Therefore, defect controlled behavior can be obtained which generates high densities of carriers even at low temperature. Especially in n-type condition which achieved in Fe-rich condition. the non-stoichiometry is mainly due to the oxygen vacancy. However the oxygen vacancy is in its neutral state at intermediate or relatively high Fermi level due to its deep nature. Instead of oxygen vacancy, Fe_I ion is dominant to the higher n-type conductivity due to its shallow nature. It also implies that the low polaron-defect ratio due to the prevailing deep oxygen vacancies highly affects low electron mobility even at intrinsic n-type condition. To avoid the low polaron-defect ratio, extrinsic doping can be a solution.

We also found that Fermi level cannot go above the electron polaron

charge transition level which is 0.55 eV below the conduction band minimum because the level works as effective band edge, thus the existence of electron small polaron affects the range of band alignment.

References

[1] R. F. G. Gardner, F. Sweett and D. W. Tanner, J. Phys. Chem. Solids **24**, 1187 (1963)

[2] Y.-H. Kim, and Y.-H. Kim, Phys. & High Tech. **9** (2012)

[3] J. P. Perdew, and W. Yue, Phys. Rev. B **33**, 8800 (1986)

[4] W. Kohn, and L. J. Sham, Phys. Rev. **140**, A1133 (1965)

[5] A.D.Becke, Phys Rev A **38**, 3098 (1988)

[6] A. I. Liechtenstein, V. I. Anisimov and J. Zaane, Phys. Rev. B **52**, R5467 (1995).

[7] G. Kresse, and J. Furthmuller, Phys. Rev. B **54**, 11189 (1996)

[8] P. E. Blochl, Phys. Rev. B **50**, 17953 (1994)

[9] NJ Mosey, P. Liao, EA Carter, J. Chem. Phys. **129**, 014103 (2008)

[10] L.A. Marusak, R. Messier, W. B. White, Phys. Chem. Solids **41**, 98 (1980)

[11] B. Gilbert, C. Frandsen, E. R. Maxey, and D. M. Sherman, Phys. Rev. B **79**, 035108 (2009)

[12] A. A. Sokol , A. Walsh, , C. R. A. Catlow, Chem. Phys. Lett. **492**, 44 (2010)

[13] K. M. Rosso, D. M. A. Smith, and M. Dupuis, J. Chem. Phys. **118**, 6455 (2003)

[14] R. H. Chang and J. B. Wagner, Jr., J. Am. Ceram. Soc. **55**, 211 (1972)

[15] A. J. Bosman and H. J. van Daal, Adv. Phys. **19**, 1(1970)

[16] J. B. Goodenough, in Progress in Solid State Chemistry, edited by

H. Reiss (Pergamon, Oxford, 1971), Vol. **5**, pp. 149.399.

[17] C. Gleitzer, J. Nowotny, and M. Rekas, Appl. Phys. A: Solids Surf. **53**, 310 (1991)

[18] C. Gleitzer, Electrical Properties of Oxide Materials (Trans Tech, Chur, Switzerland, 1997), Vols. **125** and **126**, pp. 355–417.

[19] H.-T. Jeng, G. Y. Guo, and D. J. Huang, Phys. Rev. Lett. **93**, 156403 (2004)

[20] S. Lany and A. Zunger, Phys. Rev. B **78**, 235104 (2008)

[21] H.-P. Komsa, T. T. Rantala, and A. Pasquarello, Phys. Rev.B **86**, 045112 (2012)

[22] O. N. Salmon, J. Phys. Chem. **65**, 550 (1961)

[23] A. Kudo and Y. Miseki, Chem. Soc. Rev. **38**, 253 (2009)

[24] K. Sivula, F. L. Formal, and M. Grätzel, Chem. Sus. Chem. **4**, 432 (2011)

[25] M. Catti and G. Valerio, Phys. Rev. B **51**, 7441 (1995)

[26] G. Rollmann, A. Rohrbach, P. Entel, and J. Hafner, Phys. Rev. B **69**, 165107 (2004)

[27] Z. D. Pozun and G. Henkelman, J. Chem. Phys. **134**, 224706 (2011)

국문초록

태양광을 에너지 자원으로 이용하기 위한 방안인 물의 광분해에 대한 응용에 헤마타이트(α-Fe_2O_3)가 주목 받고 있다. 헤마타이트는 지표면에 풍부하게 존재하는 산화물로서 물속에서도 안정하며 넓은 범위의 빛을 흡수하기에 적당한 밴드 갭을 (2 eV) 가지고 있다는 이점을 가지기에 물 분해로의 응용을 위한 많은 연구가 진행되고 있다. 하지만, 이 물질에 대한 많은 실험연구에 비해 이론연구, 특히 제일원리 수준의 원자적 관점의 해석은 적은 편이다. 더욱이 헤마타이트와 같은 산화물은 자연적인 점 결함에 의해 그 특성이 많이 좌우되는데도 점 결함에 대한 최근의 발전된 이론을 이용한 제일원리 연구는 거의 보고된 바 없다.

본 연구에서는 상관 시스템인 헤마타이트를 잘 기술하기 위한 DFT+U 계산법을 통해 헤마타이트의 점 결함을 연구하였다. 산소 이온과 철 이온의 공공과 침입형 결함을 모두 고려하였으며 생성에너지의 계산을 통해 상대적인 안정성을 비교해보았다. 이 때 셀의 크기에 대한 의존성을 고려하여 적합한 보정을 취한 값을 이용하였다. 각각의 결함에 의해 유도되는 전자적 결함준위가 검토되었으며 결함이 없는 결정에서의 특성과 비교하여 전자적, 공간적인 구조의 특성들을 설명하였다. 또한 점 결함이 없는 결정에서의 전자 폴라론을 결함처럼 취급하여 함께 검토하였다. 생성에너지 값을 이용해 각 점 결함의 전하상태가 전이하는 에너지 준위를 계산하였고, 결함의 농도와 페르미 준위를 전하중성조건을 이용하여 결정하였다.

이를 통하여 헤마타이트의 내인성 결함은 주로 n형 조건을 만들고, 그것이 철의 침입형 결함 때문이라는 것을 밝혔다. 이것은 헤마타이트가 자연적으로 보통 n형 특성을 갖고 있어 물 분해의 산소 발생 전극으로

이용된다는 점과 일치하는 증거이다. 또한 흥미롭게도, 전자의 폴라론의 생성으로 인해 *n*형 조건에서의 페르미 준위가 컨덕션 밴드의 바닥으로부터 0.55 eV 아래쪽으로 제한되어 있다는 점이 발견되었다. 이는 계면을 형성할 때 페르미 준위의 제어를 통한 밴드의 상대적인 준위 조정이 어느 정도로 제한되어있다는 것을 의미한다.

주요어 : 범밀도 함수이론, 점 결함, 헤마타이트, 물 분해

학 번 : 2011-20662